# A Three-Dimensional Numerical Investigation of a Carolina Coastal Front and the Gulf Stream Rainband

CHING-YUANG HUANG AND SETHU RAMAN

*Department of Marine, Earth and Atmospheric Sciences, North Carolina State University, Raleigh, North Carolina*

## ABSTRACT

A three-dimensional mesoscale planetary boundary layer (PBL) numerical model is used to investigate mesoscale circulations over the Carolina coastal and Gulf Stream baroclinic zones. Idealized ambient onshore and offshore flows are investigated, which represent the synoptic conditions during the Intensive Observation Period-2 (IOP-2) of the 1986 Genesis of Atlantic Lows Experiment (GALE). For the easterly onshore flow, a confluence zone appears west of the Gulf Stream in response to the effect of the oceanic baroclinicity. The confluence zone is nearly parallel to the coastline and the SST isotherms, with northeasterly (southwesterly) flow to the west (east). A shallow coastal front forms below 2 km as the cyclonic shear of the ageostrophic flow becomes strong. Quasi-stationary rainbands are produced by cumulus convection along the coastal front. The northern part of the front and the rainbands later encroach inland as the cold air intensity over ground weakens due to onshore warm air advection. The modeled coastal circulation is in agreement with the observations, suggesting that differential boundary-layer modification may be the main mechanism for the formation of the coastal front. The existence of an onshore ambient flow appears to be a necessary condition for the presence of the coastal front. For the northerly offshore ambient flow, the rainband therefore appears along the eastern edge of the Gulf Stream, which then moves slowly downstream in response to the generated atmospheric baroclinicity. For both flows, the development of the rainbands is sensitive to variations in eddy Prandtl number, and their growth rate can be explained in terms of conditional symmetric instability.

## 1. Introduction

Boundary-layer turbulent transfers due to air–sea temperature differences can cause significant airmass modification as the flow passes over a warmer surface. Deformation and confluence of the flow are induced in response to different degrees of modifications over regions where variations of surface temperature and roughness occur (Huang and Raman 1988, 1990; Warner et al. 1990; Wai and Stage 1989; Wai 1988). Differential heating over regions of different ground covers in general can also contribute to frontogenesis (Bluestein 1982). As maritime airflow encroaches onshore and encounters continental cold air in the winter, frontogenesis causes a distinguishable wind-shift line over the coastal region. Such an event occurred on 25 January 1986 during the Intensive Observation Period-2 (IOP-2) of the Genesis of Atlantic Lows Experiment (GALE). During this period, the eastern coastal region of the United States was dominated by a synoptic high pressure system near Maine (Fig. 1). This high pressure system provided easterly flow, which led to the formation of a coastal front over the southeast coast of the United States in conjunction with cold air damming east of the Appalachian Mountains (Richwein 1980).

Mesoscale coastal processes over the southeast coast during the IOP-2 were investigated in detail by Doyle and Warner (1990). Riordan (1990) analyzed some of the mesoscale features associated with the IOP-2 Carolina coastal front. Coastal flow in the vicinity of the Carolina coast on 25 January 1986 is given in Fig. 2. As can be seen, a prominent confluence zone forms with an axis essentially parallel to the coastline. The coastal confluence zone seems to occur not over the Gulf Stream but close to the midshelf front, a region of discontinuity in SSTs observed near the shelf break during winter (Wayland and Raman 1989). The coastal flow is frontogenetical with northerly or northwesterly flow (easterly or southeasterly flow) to the west (to the east) of the confluence axis, thus characterizing a cyclonic wind shift. This coastal front is generally shallow (below 2 km) and hence is essentially a boundary-layer phenomenon. These general features associated with the coastal front were documented by Bosart (1981) and Bosart and Lin (1984) in diagnostic analyses of the Presidents' Day Storm of February 1979. Both the GALE IOP-2 and the Presidents' Day events exhibit coastal cyclogenesis following the frontogenesis. It was hypothesized that boundary-layer heating is an important contributor to the frontogenesis and incipient cyclogenesis (Bosart 1981).

*Corresponding author address:* Dr. Sethu Raman, North Carolina State University, Department of Marine, Earth & Atmospheric Sciences, 5143 Jordan Hall, Raleigh, NC 27695-8208.
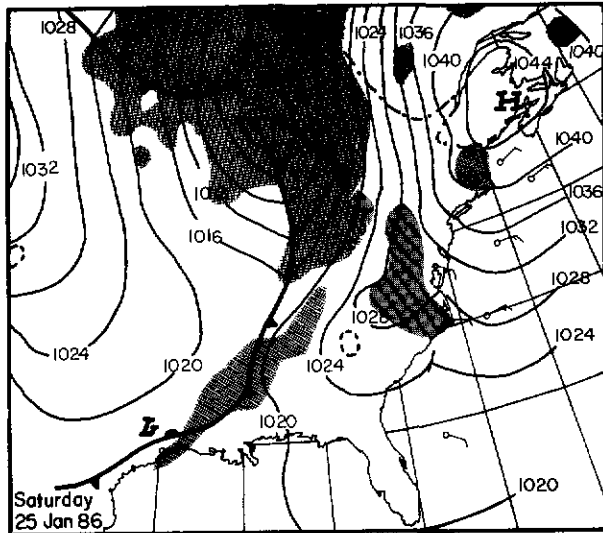
FIG. 1. The synoptic weather maps at 0700 EST
(1200 UTC) 25 January 1986.

There have been several investigations of coastal fronts over New England (e.g., Bosart 1975; Marks and Austin 1979; Nielsen 1989). Bosart (1975) analyzed the formation mechanisms of New England coastal fronts and found that differential friction plays the role of the synoptic-scale geostrophic deformation in packing the isotherms together. An initial temperature gradient must be present for the differential friction mechanism to be effective. Geostrophic deformation in itself is incapable of initiating coastal frontogenesis. Bosart's climatological studies indicated coastal frontogenesis to be associated with a pronounced cold anticyclone to the north and east of New England. This suggests the onshore flow to be a necessary condition for the coastal flow deformation and convergence. In a 3D numerical investigation of New England coastal frontogenesis, Ballentine (1980) found that eastward propagation of a synoptic-scale wave disturbance at 700 mb is a necessary but not sufficient condition for the development of a strong coastal-front circulation. He also found that the geometry and intensity of the modeled New England coastal front can be greatly influenced by many factors, but generally much less by the differential friction (surface roughness) and the Appalachian Mountains. The flow near the mountain may be significantly entrenched (toward south), but the coastal flow is primarily in response to the ocean heating (Ballentine 1980). Similar results were found in 2D numerical simulation of the Carolina coastal circulation (Huang and Raman 1990).

Although coastal fronts have been investigated numerically and observationally, their associated dynamics is still not well understood, particularly on the aspect of boundary-layer turbulent processes. Marks and Austin (1979) suggested that in New England, local precipitation enhancement could be induced by a

coastal front. The increased amount of precipitation was approximately equal to the amount of low-level moisture convergence. Cumulus convection was initiated in a shallow unstable region at the top of the warm and moist low-level flow originating over the ocean. The coastal front thus appears to be significantly related to the dynamics of mesoscale moist convection in a baroclinic zone. Dynamics of boundary-layer transfer will dominate in the coastal regions of lower latitude where oceanic baroclinicity becomes relatively stronger. Thus, there is a need to investigate the importance of differential boundary-layer momentum, heat, and water vapor transfers in the formation of a coastal front.

The objective of this paper is to investigate the formation and evolution of the 24–25 January 1986 Carolina coastal front using a 3D mesoscale model. We utilize the $E-\epsilon$ turbulence closure that combines the level 2.5 (Mellor and Yamada 1982) to determine eddy diffusivity in the boundary layer. Huang and Raman (1991a,b) showed that this hybrid scheme can reasonably simulate the turbulence structure in the marine boundary layer (MBL) over the Gulf Stream. They also found that effects of the midlevel baroclinicity above the MBL height do not change the low-level circulation significantly. It will be shown in this paper that mesoscale fronts can be initiated over the coastal baroclinic zone with significant MBL modification for onshore ambient flow. The Gulf Stream rainband is also caused by the coastal and oceanic baroclinicity, but during offshore ambient flow conditions. It is important to investigate the differences in the dynamic aspects of the MBL transfer for different ambient flow conditions since the MBL processes significantly affect the coastal cyclogeneses (e.g., Holt et al. 1990) and the initiation of Atlantic severe storms (see Dirks et al. 1988). We first present the numerical results of the simulated coastal front and the Gulf Stream rainband in sections 3 and 4, respectively. In section 5, some major factors that influence the mesoscale circulations are discussed. Conclusions are given in section 6.

## 2. Model descriptions and the numerical experiments

The mesoscale numerical model used in this study is identical to that in Huang and Raman (1991a,b). A complete description of the model is given by Huang (1990). The model is hydrostatic and anelastic in a terrain-following coordinate system. The model physics includes cloud microphysics that follows Kessler's formulations (Kessler 1969). To account for advection effects, a modified version of the Warming–Kutler–Lomax (WKL) advection scheme (Warming et al. 1973) is used in the horizontal and the quadratic upstream interpolation in the vertical. The two schemes are at least third-order accurate (see Huang and Raman 1991c). A turbulence closure scheme based on two prognostic equations, one for the turbulent kinetic en-
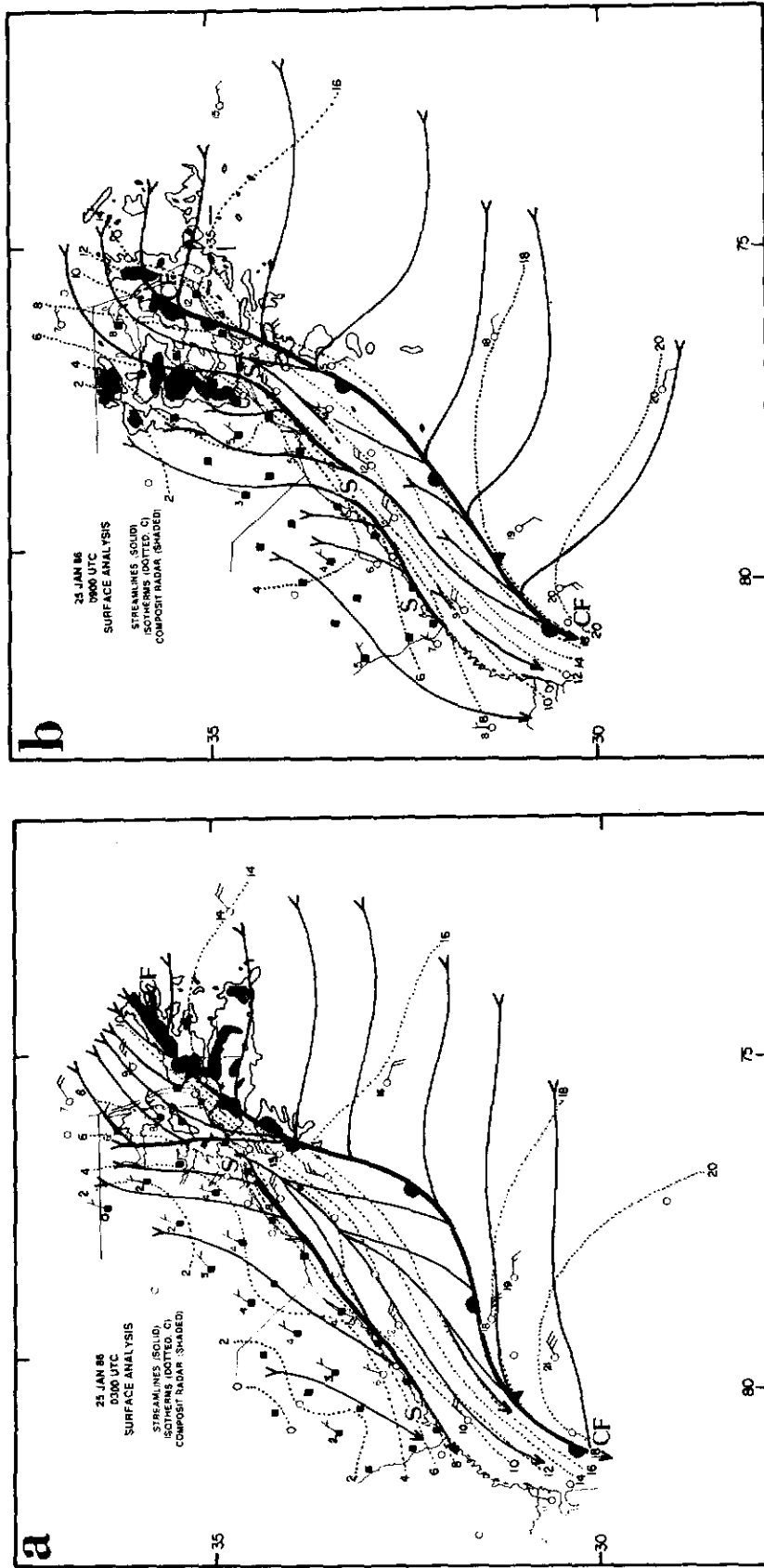
FIG. 2. Surface streamline (solid lines) and isotherm analysis (dotted lines, labeled in °C) for (a) 0300 and (b) 0900 UTC 25 January (after Riordan 1990).

ergy (TKE) and the other for turbulent energy dissipation ($\epsilon$), is incorporated with the level 2.5 formulation of Mellor and Yamada (1982) to determine eddy diffusivity (see Huang and Raman 1991a). All vertical diffusion terms are computed by a time-implicit scheme that allows the model to use a time step that is not constrained by turbulent diffusion (Huang and Raman 1988).

The geographic region for simulation is shown in Fig. 3 and is indicated by the bold lines. The model domain covers the coasts of North and South Carolina and the Gulf Stream meander. For better horizontal resolution, the Appalachian Mountains were not included in the model domain since the mountain influence has been found to be of secondary importance in the dynamics of the coastal circulations of the eastern United States (Bosart 1975; Ballentine 1980; Huang and Raman 1990; Lin 1990).

Figure 4 depicts the distribution of the observed SSTs in the simulated region. Sea surface temperatures far downwind of the Gulf Stream have been assumed to be uniform in this study. As can be seen, the SST contours are closely aligned with the coastline. The Gulf Stream core extends northeastward from the middle of the southern domain boundary, with a maximum temperature of about 25°C. The midshelf front can be identified as a region of large SST gradients at an offshore distance of about 70 km. The SSTs are assumed to be fixed during the simulated period (about one-half day). Since a uniform observed temperature of 2°C is used initially (as indicated in Fig. 2), the air-
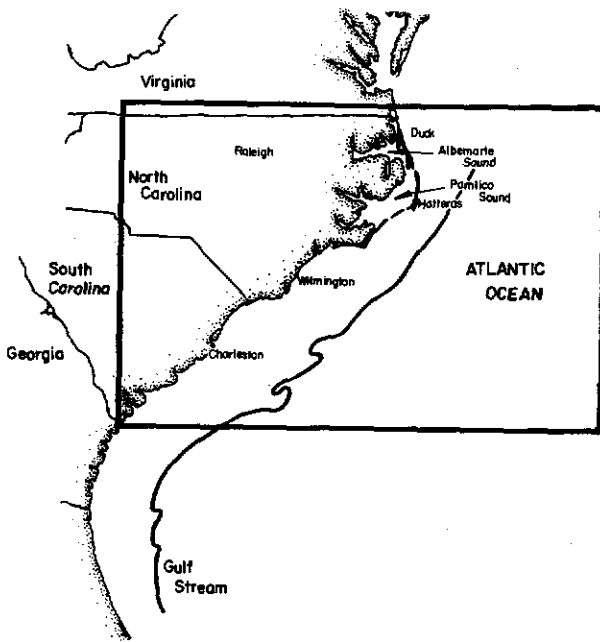


SURFACE TEMPERATURE (°C)

CONTOUR MIN = 2.0000
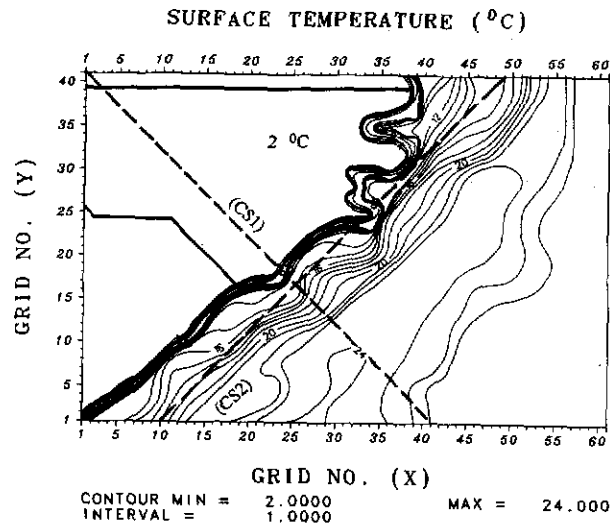INTERVAL = 1.0000          MAX = 24.000

FIG. 4. Initial ground and sea surface temperatures (in °C). Heavy lines indicate the borders of the three states, Virginia, North Carolina, and South Carolina, and two dashed lines are for the cross section 1 (CS1) and the cross section 2 (CS2) used in the text.

sea temperature difference over the Gulf Stream core can be as large as 23°C. This large air-sea temperature contrast would result in the development of a highly convective MBL. As the turbulent heating in the MBL reaches a quasi-equilibrium stage, this air-sea temperature difference over the Gulf Stream core, however, decreases to 10°C or less, in agreement with the observations (Wayland and Raman 1989; Riordan 1990).

Vertical sounding observations over water were sparse for a scale of 200 km. Lack of mesoscale data resolution over water, therefore, makes real case simulations difficult. Upstream ambient conditions are used instead to specify initial flow based on the Ekman-gradient wind equations (see Huang and Raman 1988). Four cases are simulated in this study. A description of these cases is given in Table 1. Case ON1 is for the easterly flow, case OF1 for the northerly flow, and cases ON2 and OF2 are for their corresponding



FIG. 3. The geographical region (indicated by bold lines) considered for 3D simulations.

TABLE 1. Numerical experiments for the two events of the 1986 GALE IOP-2, case ON1 for coastal front and OF1 for the Gulf Stream rainband. Cases ON2 and OF2 use ON1 and OF1 case results at 6 h as the initial conditions, respectively.

| Case | PBL closures | Geostrophic wind (m s$^{-1}$) | Integration time (h) |
|------|-------------|-------------------------------|----------------------|
| | | Onshore flow | |
| ON1 | $E-\epsilon$ (Pr$_t$ = 1) | $U_g = -7.5$, $V_g = 0.1$ | 0–15 |
| ON2 | $E-\epsilon$ (Pr$_t$ not assumed) | $U_g = -7.5$, $V_g = 0.1$ | 6–12 |
| | | Offshore flow | |
| OF1 | $E-\epsilon$ (Pr$_t$ = 1) | $U_g = 0.1$, $V_g = -7.5$ | 0–12 |
| OF2 | $E-\epsilon$ (Pr$_t$ not assumed) | $U_g = 0.1$, $V_g = -7.5$ | 6–12 |

sensitivity tests on turbulence closure. Barotropic ambient conditions are assumed initially for all simulations, with a constant vertical potential temperature gradient of 4°C km$^{-1}$ and an 80% relative humidity below 1 km. The relative humidity is assumed to decrease linearly to zero at 5-km height. The 2D modeling studies (Huang and Raman 1988, 1991b) indicate that the MBL front may be solely induced by low-level differential turbulent heating and is less influenced by upper-level baroclinicity and moistening. Low-level wind speed and initial air–sea temperature differences appear to be two dominant factors in the development of the regional circulation.

The mesoscale model is initialized based on a 1D PBL model solving the Ekman–gradient wind equations for the flow over ground. During the model integration, ground temperature is set to be equivalent to the surface-layer air temperature (at 50-m height), but over ocean SSTs are held constant. Since diurnal variations are neglected in all the simulations for simplicity, an average ground temperature of 2°C observed at the time that the coastal front begins to form is used. Diurnal effects may play a role in the inland movement of the coastal front as was found in the 2D simulations (Huang and Raman 1990). For 3D flow over a limited area, lateral boundary conditions become more critical for realistic determination of diurnal variations.

The model horizontal domain includes 61 × 41 grids with a uniform grid interval of 12.5 km (Fig. 4). Non-staggered variables are defined on grids for all of the case simulations. The time steps for integration are 20 s for advection and 40 s for all other model physics. There are 16 grids in the vertical with the model top at a height of 8 km. Although coastal fronts are essentially shallow, frontal rainbands could develop much higher than the depth of the front itself. Observations indicate that the Gulf Stream rainbands can be 6 km high (Sienkiewicz et al. 1989).

For all simulations, zero gradient conditions are used at the lateral boundaries (a radiation condition of the Orlanski type was tested and found to produce artificial thermal gradients at the model oceanic boundaries where wave speeds cannot be easily determined). To minimize the thermal gradients that are possibly generated due to the imposed boundary conditions, the first-order upstream scheme is applied at grids closest to the lateral boundaries. At the upper boundary, a radiation boundary condition (Klemp and Durran 1983) is used to determine the upper perturbation pressure. This radiation condition allows outward propagation of wave energies.

## 3. Easterly ambient flow: Coastal front

Easterly onshore flow is associated with a high pressure system situated northeast of the Carolina coastal region (see Fig. 1). Case ON1 is designed to investigate the coastal confluence resulting from this onshore flow

condition with a surface wind speed of 7.5 m s$^{-1}$. This ambient wind is used as the model geostrophic wind, which is assumed to be constant with height. Figure 5 shows the time evolutions of domain maximum and minimum vertical velocities and domain maximum surface-layer wind speed for the case ON1. As can be seen in this figure, the system develops rapidly after 7–8 h of ocean warming. Similar system development was also found in the 2D simulations for the cold air outbreak (Huang and Raman 1991b). The updrafts reach maximum velocities at 8.5 model integration hours and are much stronger than the downdrafts. Similar results were obtained for the 2D cases as well (Huang and Raman 1991b). It will be shown later that the fastest development of the updrafts is related to cloud formation associated with the release of latent heat. Variation of the maximum surface-layer wind speed is similar to that of the updrafts, particularly before the mature stage (about 10 h). This indicates that the development of the updrafts and the clouds is mainly in response to low-level convergence. In general, the surface-layer flow keeps intensifying with time, but
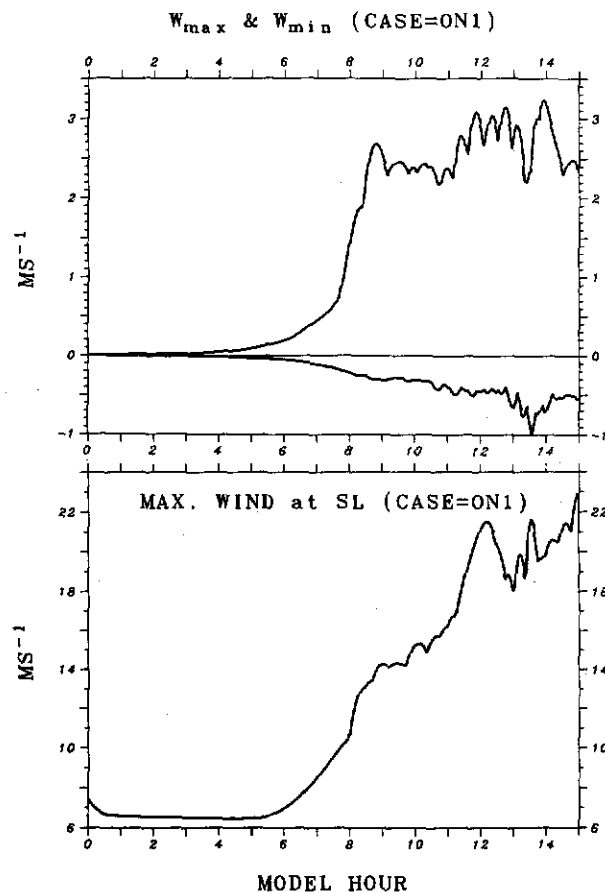


FIG. 5. Time evolutions of oceanic domain maximum vertical velocity and minimum vertical velocity (upper panel) and maximum surface-layer wind speed (lower panel) for case ON1 (easterly ambient flow).

the updrafts cease to grow after about 9 h. Later increase in the surface-layer wind speed is caused by the increased low-level convergence. Salient features and dynamics associated with the coastal circulation are discussed below.

### a. Coastal circulation

Patterns of the evolving coastal flow near the surface are given in Fig. 6. As can be seen, the coastal flow becomes confluent south of Albemarle and Pamlico by 6 h. The confluence axis is close to the coastline, and they are primarily parallel to each other (Fig. 6a). At 9 h, a weak diffluence zone appears just ahead of the Pamlico Sound, with some local convergence zones of shorter scale east of the confluence axis (Fig. 6b). These shortwave structures tend to diminish with time, as were found in the calm wind conditions (Warner et al. 1990). The flow west of the confluence zone turns southward as it responds to locally generated pressure gradients due to different boundary-layer modifications over ground and the ocean. Similarly, the flow southeast of the zone turns northward. In response to the frontogenetical flow, the confluence axis becomes more discernible at 12 h (Fig. 6c). The southern portion of the axis migrates offshore with time and finally attaches to the western edge of the midshelf front (Fig. 6d). The offshore migration of the southern confluence axis can also be seen in cross-sectional results to be presented later. At 15 h, the easterly flow just offshore of South Carolina (a region of the Gulf Stream core) becomes normal to the coastline.

The flow pattern with a cyclonic wind-shift line is favorable for maximizing the coastal frontogenesis since this line (acting as an axis of dilatation) is almost along the isotherms (Petterssen 1936), similar to the New England coastal frontogenesis (Bosart 1975). Ageostrophic wind (or isallobaric wind) is thus accelerated toward the front, with a speed of about 20 m s$^{-1}$, considerably larger than the ambient geostrophic wind speed (7.5 m s$^{-1}$). Warner et al. (1990) found that in calm wind conditions associated with a maximum air-sea temperature difference of about 10°C, a maximum wind speed of 7.40 m s$^{-1}$ can be produced in the MBL convergence zone. The ageotrophic coastal frontogenesis differs from the process of geostrophic deformation in a synoptic cold front.

The model results compare well with the observational analyses (Fig. 2). More details of the observational analyses can be found in Doyle and Warner (1990) and Riordan (1990). The simulated flow between 9 and 12 h is similar to the observed flow pattern at 0300 UTC 25 January 1986, and the flow between 12 and 15 h is in better agreement with the observations at 0900 UTC of the same day. Since the model simulation relies on one sounding initialization and the mesoscale circulation takes time to spin up, actual phase of the flow cannot be exactly modeled. In the real case, direction of the far upstream ambient flow also changes with time. However, reproduction of the observed coastal flow pattern tends to substantiate the hypothesis that boundary-layer effects play the most important role and may be solely responsible for the formation of the coastal front.

Several explanations exist for coastal frontogenesis. Bosart (1975) found that the New England coastal frontogenesis can be explained in terms of differential surface friction between land and ocean. Bosart (1981) later discussed the importance of the differential boundary-layer heating in the Carolina coastal frontogenesis of the Presidents' Day Storm. For the same case, Bosart and Lin (1984) found that frontogenesis responds to differential boundary-layer warming and moistening in conjunction with sensible heating over the ocean and the blocking of shallow cold air by the Appalachian Mountains. Doyle and Warner (1990) showed the important effects of both ageostrophic deformation and differential diabatic heating for the GALE IOP-2 event. Based on numerical results, Ballentine (1980) related the New England coastal frontogenesis mainly to the ocean heating associated with turbulent mixing in the MBL. In our case, the Carolina coastal circulation is initiated by the effect of the strong oceanic baroclinic zone. The development of the modeled coastal front is apparently a result of differential boundary-layer modification between the land and the ocean.

With the advection effects of the onshore flow, surface air temperature near the northern coastline has been warmed up to 7°C or higher at 15 h (see the dashed lines in Fig. 6d). Larger surface warming is associated with the deeper inland penetration of the veering maritime flow. In contrast, the southern coastal baroclinic zone maintains its initial intensity because of the cold air advection associated with the north-northeast wind west of the front. By this time, the North Carolina part of the coastal confluence zone has migrated slightly inland due to the weakening of the cold air intensity over ground, while its South Carolina part remains near the same location. These structural features of the coastal front are consistent with the observations (Riordan 1990).

To understand the vertical structure of the coastal flow, cross-sectional results are examined. Two cross sections are selected (they are indicated by the two heavy dashed lines in Fig. 4). The first cross section (CS1) is a plane from the northwestern corner to the 41st grid in the east–west direction, and the second cross section (CS2) is a plane along the midshelf front. Figure 7 depicts the wind fields at 12 and 15 h for CS1. Note that in this figure the positive horizontal ordinate is approximately toward the southeast and the coastline is located on grid 23. The contour lines represent the wind component normal to the plane, with positive (negative) values indicative of its direction into (out of) the paper. Vectors are for the vertical velocity and
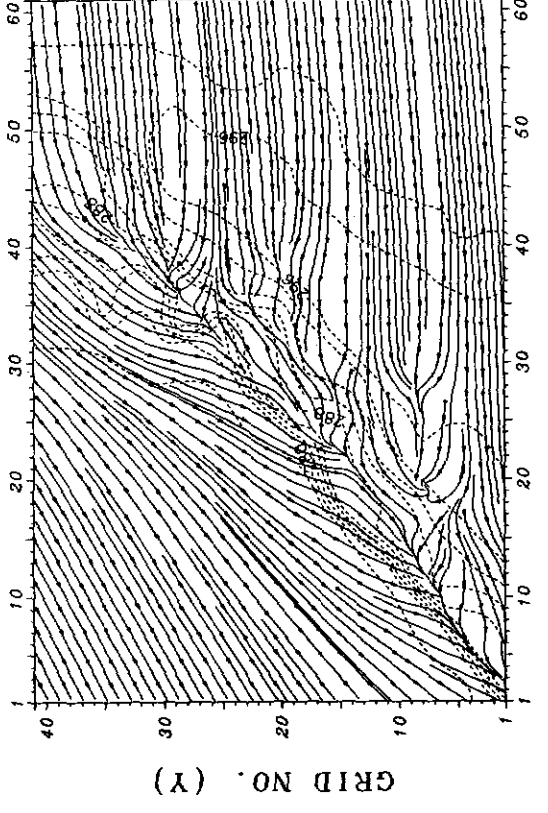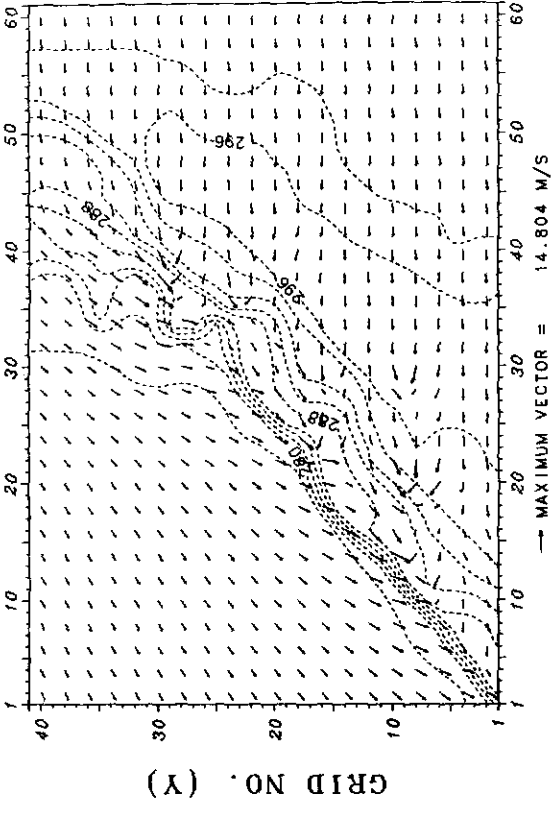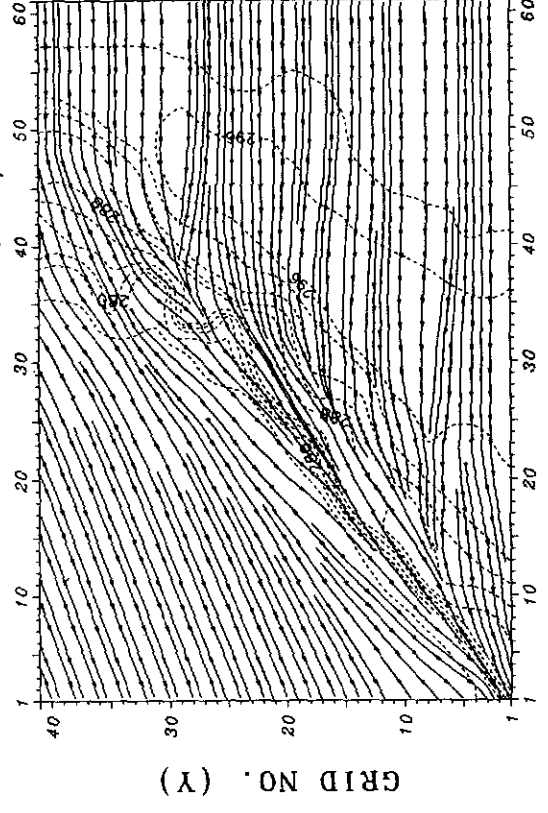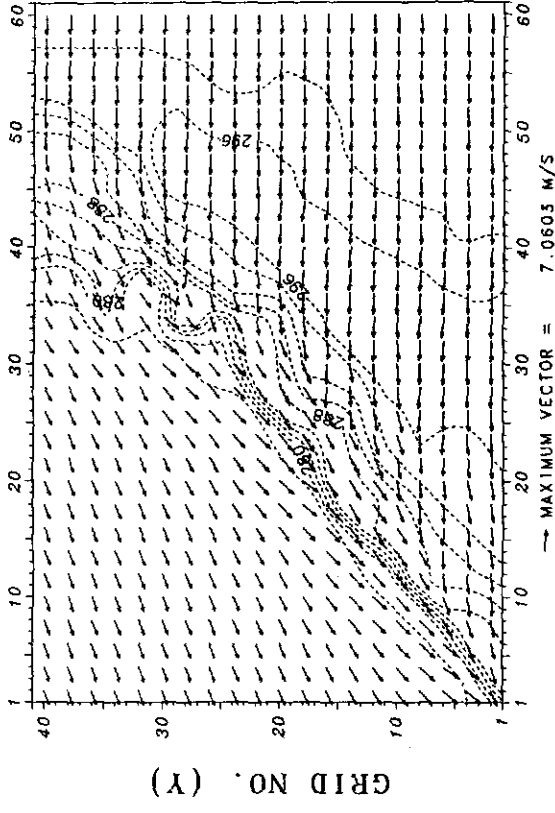
FIG. 6. The results for $u$ and $v$ and their streamlines at 150 m AGL for the case ON1 at (a) 6 h, (b) 9 h,

U & V (CASE=ON1, Z=150 M, HR=15)

GRID NO. (Y)

MAXIMUM VECTOR = 20.441 M/S
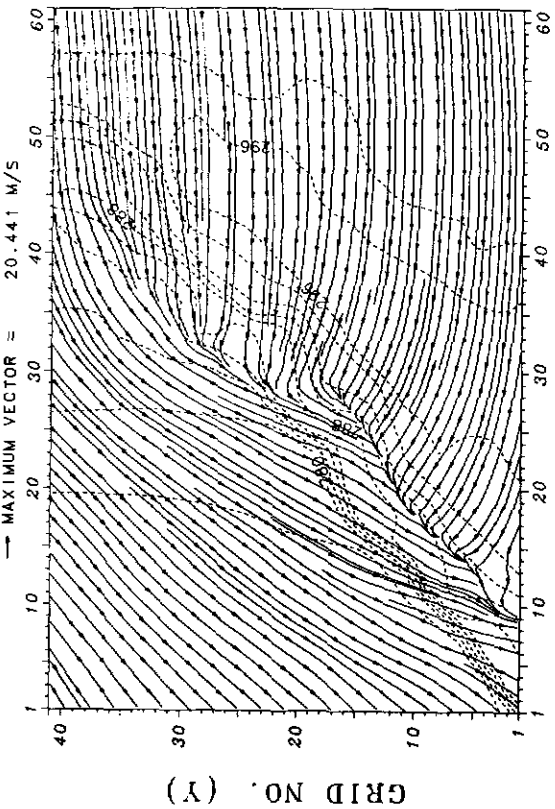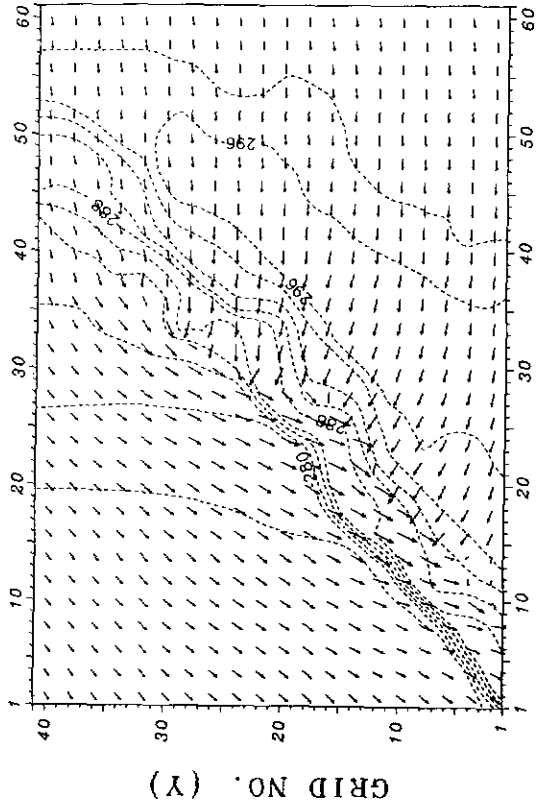
GRID NO. (X)

GRID NO. (Y)

U & V (CASE=ON1, Z=150 M, HR=12)

GRID NO. (Y)

MAXIMUM VECTOR = 19.391 M/S
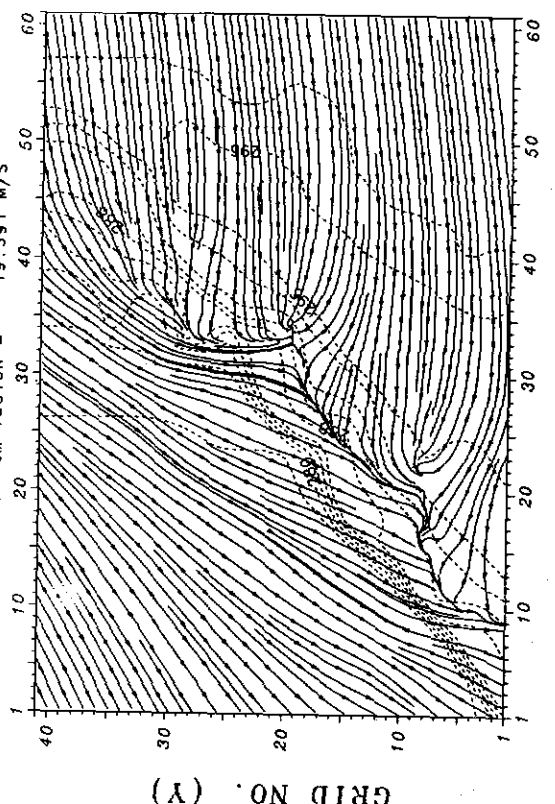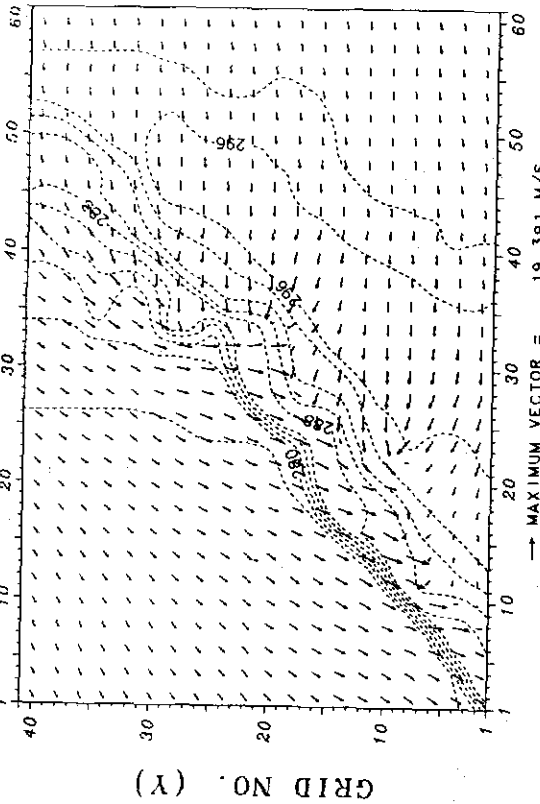
GRID NO. (X)

GRID NO. (Y)

FIG. 6. (*Continued*) (c) 12 h, and (d) 15 h. Maximum magnitude of the wind is plotted under the frame. The surface temperatures are indicated by dashed contour lines with an interval of 2 K.

FIG. 7. The results for the wind fields at the cross section 1 (CS1) at 12 and 15 h for case ON1. Positive *x* is to the right (roughly normal to the coastline). Maximum wind component along the cross sect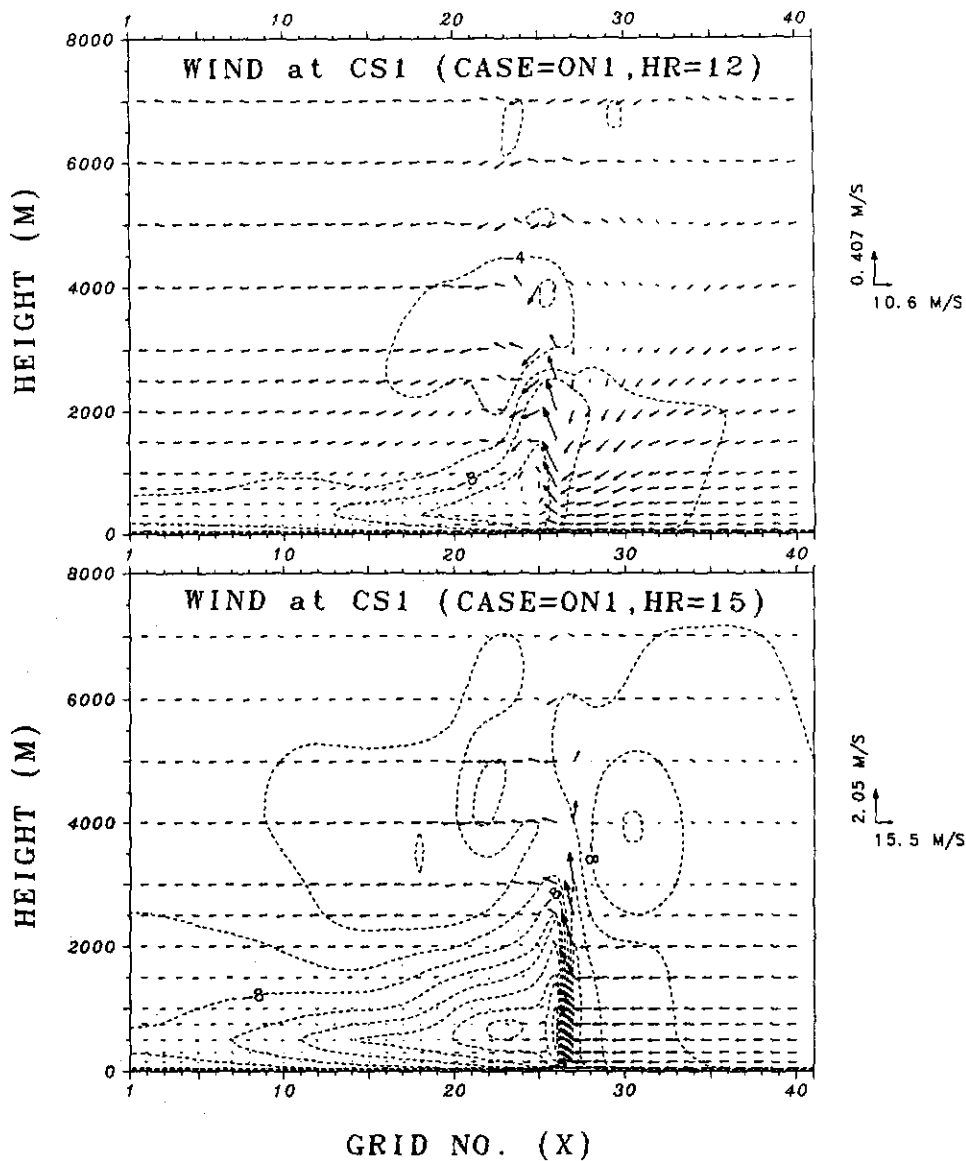ion and maximum vertical velocity are plotted at the right-hand side of the frame. Contour interval for the wind component perpendicular to CS1 is 2 m s⁻¹.

the wind component along the cross section. As can be seen, strong low-level wind convergence occurs at some distance offshore, with reversed flow (offshore) just west of the convergence zone. The location of the convergence zone migrates offshore with time and is situated at an offshore distance of about 50 km by 15 h. The horizontal wind patterns at 12 h (not shown) reveal that coastal flow at 1-km height is still confluent along the low-level confluence axis, but becomes diffluent at 2-km height. The flow confluence continues to develop to a height of 2 km at 15 h.

At the leading edge of the accelerated near-surface flow, a significant updraft develops in response to the

low-level convergence in the frontal zone. The updraft develops with time and reaches to a height of 6 km at 15 h. This updraft does not tilt with height in a barotropic ambient environment, similar to that in breeze circulation fronts (Huang and Raman 1988). An outflow jet appears to the left of the upper-level updraft. The developed height of the flow confluence is just beneath the level of the outflow. Strongest diffluence (or divergence) occurs at the level of the outflow jet. The second cross-sectional (CS2) results indicate that the northwest wind west of South Carolina coastline develops to a height of only 3 km at 15 h (not shown). The divergence due to the outflow prevents the upward

development of the frontogenetical shear. This effect is associated with the vertical tilting that contributes to the largest frontolysis. In general, the structural features of the 3D coastal front are similar to those of the 2D front (Huang and Raman 1990).

Equivalent potential temperature $\theta_e$ and equivalent potential vorticity $q_e$ for CS1 are shown in Fig. 8 to present results on the frontal thermodynamic variation. A shallow frontal structure forms just offshore of the coastline (grid 23), as is evident in the low-level packed isentropics. Moistures in the frontal zone can be transported upward to 5 km. Also, a moisture tongue extends inland over the front, penetrating to a distance more than 100 km. The potential temperature fields (not shown) indicate that the front is rather shallow (below 2 km). Release of the latent heat over the front, however, can largely contribute to the development of cumuli as indicated by the well-diffused $\theta_e$ in the vertical. Another important feature is the similarity between the distributions of $\theta_e$ and $q_e$. As can be seen, negative $q_e$ appears in convective instability regions



FIG. 9. The results for cloud water $q_c$ and rainwater $q_r$ at 2.5 km AGL at 9 h for case ON1. Dashed lines are for surface potential temperature. Contour intervals are 0.05 g kg$^{-1}$ for both $q_c$ and $q_r$.

where $\partial\theta_e/\partial z$ is negative. Equivalent potential vorticity $q_e$ can be used as an indicator for stability diagnosis of the flow to be discussed later.

At the time of six model integration hours, a considerable amount of clouds has formed over the convergence zone but rainwater is still negligible (not shown). Cloud-water loading has a maximum value just offshore of Pamlico Sound and increases only slightly at 9 h. As flow confluence south of the sound becomes stronger (see Fig. 6c), cloud waters at other places of flow convergence have increased significantly (Fig. 9). The distributions of the cloud waters are somewhat irregular, but roughly aligned with the coastline. Largest rains (with a magnitude of 0.85 g kg$^{-1}$), however, appear offshore of South Carolina and modest rains occur over Pamlico Sound. Rain activities in the vicinity of North Carolina coast were detected by National Weather Service radars (see Doyle and Warner 1990; Riordan 1990).

For a better understanding of configurations of the cloud and rain water, their 3D structures at 9 h are
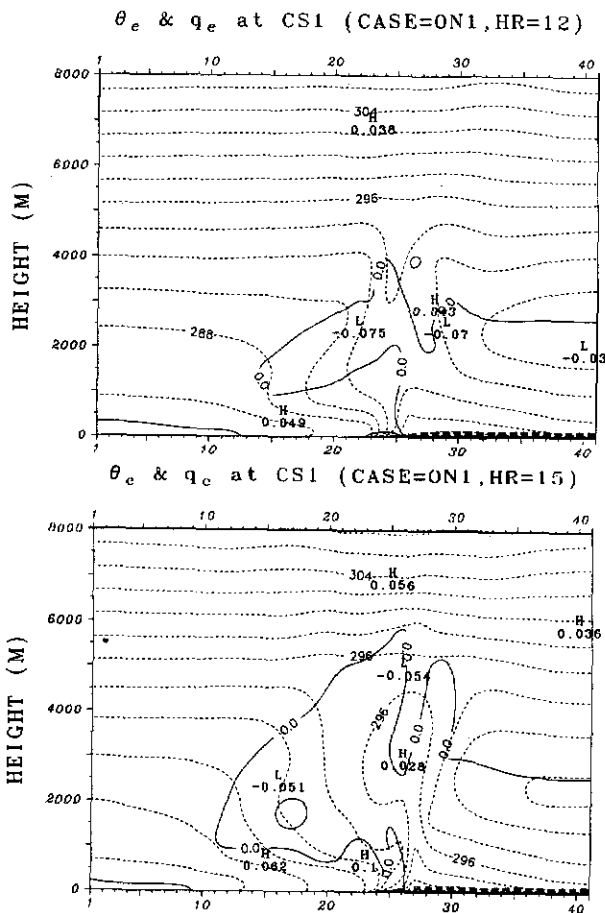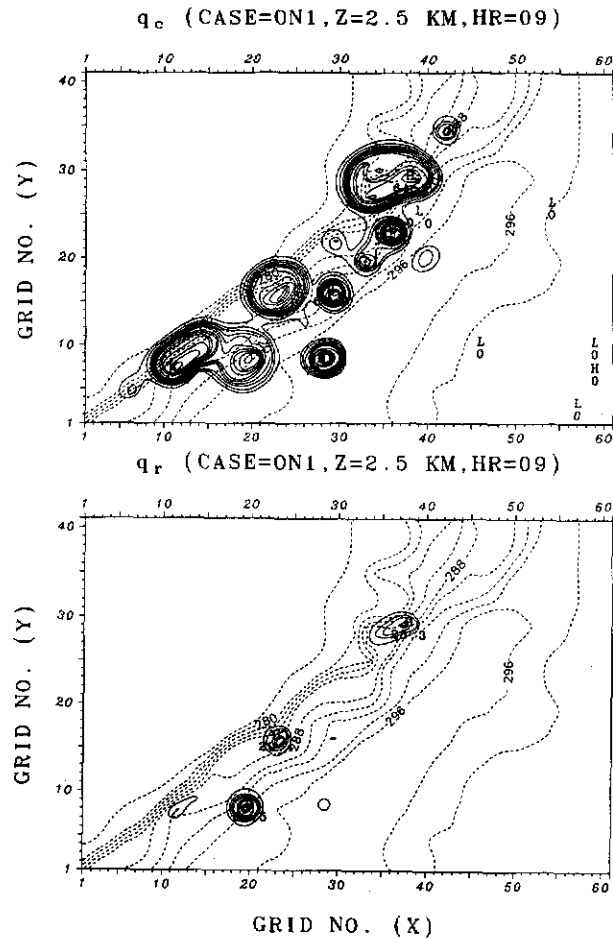


FIG. 8. As in Fig. 7 but for equivalent potential temperature $\theta_e$ (shorter dashed lines) and equivalent potential vorticity $q_e$ (longer dashed and solid). Contour intervals are 2 K for $\theta_e$ and $10^{-5}$ K m$^{-1}$ s$^{-1}$ for $q_e$. See text for the definition of $q_e$.

plotted in Fig. 10. In this figure, one grid box indicates a volume of 12.5 km × 12.5 km × 500 m. Larger clouds and rains appear over the region with stronger flow convergence. In general, cloud and rain water are distributed along the confluence axis. The rainwater forms in a band-shaped structure, but broken at places due to local diffluence and divergence. The average height of the cloud and rain water at 12 h is about 5–6 km. At later times, the rainband becomes wider and higher (close to the model top), as shown in Fig. 11. The northern part of the cloud and rain bands (near Pamlico Sound) encroaches somewhat inland with time, while their southern part remains almost stationary.

### b. Turbulent transfer

As aforementioned, differential boundary-layer modification may be responsible for the formation of the coastal front. It would be appropriate to discuss the effects of turbulent transfer before presenting a detailed analysis of the coastal frontogenesis. The distributions of surface-layer turbulent sensible and latent heat fluxes at 12 h are shown in Fig. 12. Over ground, there is no surface sensible heat flux due to the imposed neutral surface layer that, however, can still yield small
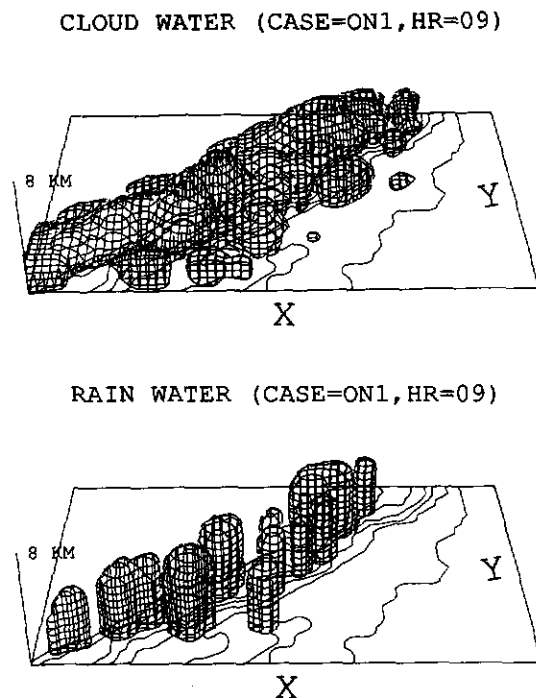
RAIN WATER (CASE=ON1,HR=12)

RAIN WATER (CASE=ON1,HR=15)



FIG. 11. As in Fig. 10 but for rainwater at 12 and 15 h.

CLOUD WATER (CASE=ON1,HR=09)

RAIN WATER (CASE=ON1,HR=09)



FIG. 10. Three-dimensional configuration of cloud water $q_c$ and rainwater $q_r$ (both greater than 0.01 g kg$^{-1}$) at 9 h for case ON1. Contour lines (with an interval of 2 K) on the plane of $z = 0$ are for the sea surface temperature. The horizontal domain size is identical to that in Fig. 4. One gridbox size in the enveloped volume of the cloud- and rainwater is equivalent to 12.5 km × 12.5 km × 500 m.

latent heat flux. Over the ocean, regions of maximum total surface turbulent heat fluxes (sensible and latent) are located near the western edge of the Gulf Stream core, that is, the eastern edge of the convergence zone. Maximum heating is not produced at the regions of the largest initial air–sea temperature difference for the onshore flow. Indeed, this feature exists also for calm wind conditions (Warner et al. 1990), indicative of the importance of the low-level accelerated wind in determining turbulent heat transfer. The latent heat flux closely resembles the sensible heat flux in spatial distribution, but with magnitudes about 2–3 times larger. In general, the distributions of the sensible and latent heat fluxes primarily follow the SST isotherms, except for some regions with maximum heat fluxes caused by local flow convergence just ahead of the front. It should be noted that the distribution of the modeled heat fluxes based on Monin–Obukhov surface-layer similarity theory differs somewhat from the observational results using the bulk aerodynamic method. But, values of the modeled total heat fluxes over the frontal region (around 600–800 W m$^{-2}$) compare favorably with the observations during the period (Doyle and Warner 1990). The modeled sensible heat flux (about 200–400 W m$^{-2}$) and its distribution west of the Gulf Stream are also in agreement with the observations from meteorological buoys showing a maximum value of about 240 W m$^{-2}$ (Riordan 1990).

The distribution of total turbulent heat fluxes exhibits two zones with significant gradients for the on-
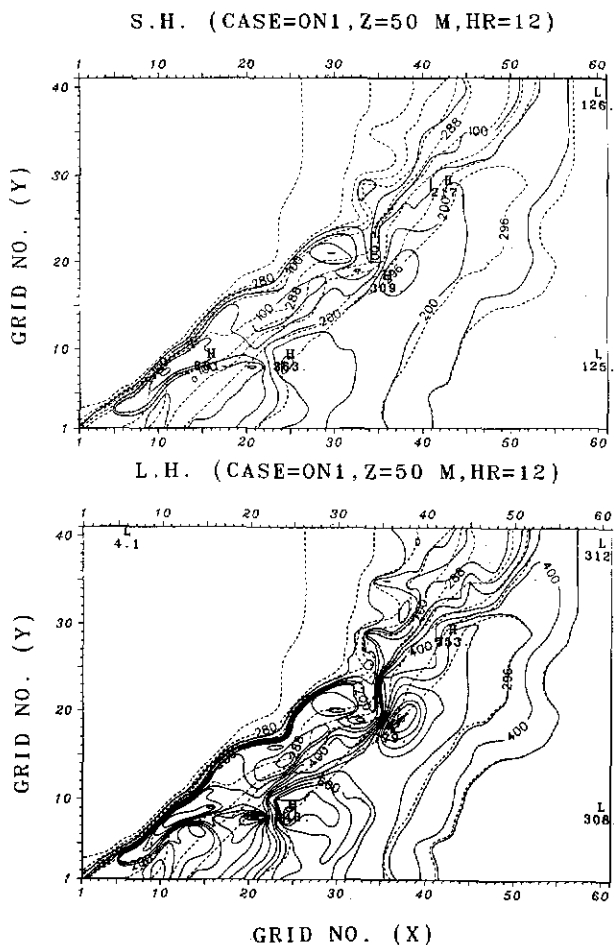
S.H. (CASE=ON1,Z=50 M,HR=12)



L.H. (CASE=ON1,Z=50 M,HR=12)



GRID NO. (X)

FIG. 12. The results for the surface-layer turbulent sensible and latent heat fluxes at 12 h for case ON1. Contour intervals are 50 W m$^{-2}$ for both heat fluxes.

adjacent to the 23°C SST contour; they are referred to as three important heating nodes. Nodal structures of maximum heating were also found in the model simulations with calm wind conditions (Warner et al. 1990). Except for the southern node offshore of South Carolina, both the northern one (offshore of the North Carolina sounds) and the middle one were observed at 0000 UTC 25 January 1986 (Riordan 1990; Doyle and Warner 1990). The southern node, however, is the strongest with total heat fluxes up to 1300 W m$^{-2}$. Location of the confluence axis (Fig. 6d) between the Gulf Stream core and the coastline appears to be in response to large differential heating in the vicinity of the midshelf front. This result was also found in the 2D simulations (Huang and Raman 1990). The warmest Gulf Stream core does not necessarily imply a region of maximum differential heating and hence, does not lead to prominent frontogenesis. However, the Carolina coastal front is located farther offshore compared to the New England coastal front. This could be attributed to the joint baroclinicities of the midshelf front and the Gulf Stream.

The PBL height over ground is constrained below 1 km during the integration period, while the MBL develops up to about 3 km by 15 h as indicated by the turbulent kinetic energy (TKE) budgets (not shown). Near the surface, buoyancy production due to surface heating is primarily balanced by turbulent transport and dissipation. The near-surface buoyancy production is large over the frontal zone with a value of about 0.008 m$^2$ s$^{-3}$ and decays almost linearly with height, characteristic of a convective boundary layer. The resulting difference between the boundary layers over land and the ocean leads to coastal frontogenesis. Analyses of coastal frontogenesis are given below.

shore flow, one along the coastline and the other west of the Gulf Stream core, near the region of the midshelf front. There are also three maximum heat flux regions

*c. Analyses of frontogenesis*

Frontogenesis can be analyzed with the aid of a frontogenetical function defined as

$$F = \frac{D}{Dt} |\nabla\theta|$$

$$= \frac{1}{|\nabla\theta|} \left\{ \frac{\partial\theta}{\partial x} \left[ -\frac{\partial u}{\partial x}\frac{\partial\theta}{\partial x} - \frac{\partial v}{\partial x}\frac{\partial\theta}{\partial y} - \frac{\partial w}{\partial x}\frac{\partial\theta}{\partial z} + \frac{\partial}{\partial x}\left(\frac{d\theta}{dt}\right) \right] + \frac{\partial\theta}{\partial y} \left[ -\frac{\partial u}{\partial y}\frac{\partial\theta}{\partial x} - \frac{\partial v}{\partial y}\frac{\partial\theta}{\partial y} - \frac{\partial w}{\partial y}\frac{\partial\theta}{\partial z} + \frac{\partial}{\partial y}\left(\frac{d\theta}{dt}\right) \right] \right\} \quad (1)$$

$$\qquad\qquad 1 \qquad\qquad 2 \qquad\qquad 3 \qquad\qquad 4 \qquad\qquad\qquad 5 \qquad\qquad 6 \qquad\qquad 7 \qquad\qquad 8$$

to which contributions are horizontal deformation or flow confluence (terms 1, 2, 5, and 6), tilting effects (terms 3 and 7), and differential diabatic heating (terms 4 and 8). Diabatic effects in the model simulation include turbulent heat transfer, latent heat release, and evaporation of rainwater. For the near-surface flow, turbulent heat transfer would dominate. We will focus on the near-surface frontogenesis since the modeled circulation is driven by the surface temperature gra-

dients. In the evaluation of the near-surface differential turbulent heating, the latent heat flux is not included, although low-level moisture flux does contribute in part to the cloud formation.

Figure 13 shows the results for the three frontogenetic components and the total frontogenesis at a height of 150 m at 12 h. Maximum frontogenetical contribution is caused by horizontal deformation (or flow conflu-

### T1256 (CASE=ON1,HR=12,Z=150 M)



GRID NO. (X)

CONTOUR MIN = -5.0000          MAX = 34.000
INTERVAL = 1.0000

### T48 (CASE=ON1,HR=12,Z=150 M)



GRID NO. (X)

CONTOUR MIN = -18.000          MAX = 20.000
INTERVAL = 1.0000

FIG. 13. Frontogenetical analyses for the model results at 150 m AGL at 12 h. (a) The horizontal deformation (terms 1, 2, 5, and 6), (b) the differential turbulent sensible heating (terms 4 and 8),

T37 (CASE=ON1,HR=12,Z=150 M)



CONTOUR MIN =   −3.0000      MAX =   12.000
INTERVAL =      1.0000

F (total) (CASE=ON1,HR=12,Z=150 M)



CONTOUR MIN =   −11.000      MAX =   28.000
INTERVAL =      1.0000

FIG. 13. (*Continued*) (c) the tilting effect (terms 3 and 7), and (d) total frontogenesis. In all the figures, solid lines indicate frontogenesis while long dashed lines are for frontolysis. Frontogenetical contour interval is $1°C (100 \text{ km})^{-1} \text{ h}^{-1}$. Potential temperature at this height is also plotted for reference (represented by short dashed lines in a contour interval of $1°C$).

ence) up to 34°C $(100 \text{ km})^{-1} \text{ h}^{-1}$, while the tilting effects are smallest except at the regions of the three heating nodes mentioned before. Tilting effects induce frontogenesis along the leading edge of the front, because $\partial w / \partial x$ is positive and $\partial\theta / \partial z$ is negative near the surface. Frontogenesis due to differential turbulent heating [with a maximum of 20°C $(100 \text{ km})^{-1} \text{ h}^{-1}$] does not exceed that by flow confluence, in agreement with the observational analyses (Doyle and Warner 1990). Flow confluence produces regions of larger frontogenesis rate, most of which are along the midshelf front, in support of the alignment of the rainbands shown in Fig. 11. On the other hand, differential turbulent heating gives stronger frontogenesis along the coastline south of the Carolina sounds and offshore frontolysis to the west of the midshelf front. The offshore frontolysis just west of the confluence axis is not in agreement with the observational analyses (Doyle and Warner 1990), which show moderate frontogenesis over this coastal baroclinic zone. It is interesting to note that the contribution to frontogenesis by this component is minimum in the vicinity of the North Carolina sounds, indicative of the combined effects of the relatively cold water fetch and advection of the maritime flow discussed before. Atmospheric baroclinicity in the northern coastal region is considerably less than that in the southern region (Fig. 13c). The total frontogenesis (Fig. 13d), hence, is mainly the combination of these two parts, showing two frontogenetical banded structures, one along the southern coastline and the other along the northern midshelf front. The two frontogenetical bands are not conjoint, which could be the reason for the separation of the coastal front at a later time (Fig. 6c).

The estimated maximum frontogenesis from the observations during the formation period of the coastal front is about 4°C $(100 \text{ km})^{-1} \text{ h}^{-1}$ (Doyle and Warner 1990), which is nearly four times larger than in the coastal front of the Presidents' Day Storm (Bosart and Lin 1984) and about seven times smaller than the values in this study and in Ballentine (1980). Despite these differences in the numerical values, a close similarity exists in the flow patterns and magnitudes of surface turbulent heat fluxes. Considering that the maximum variation of $\partial u / \partial x$ is $\sim 8 \text{ m s}^{-1}$ and $\partial\theta / \partial x$ $\sim 1.4°C (10 \text{ km})^{-1}$ in Fig. 7, one can easily find that coastal frontogenesis solely due to the flow confluence can be as large as 30°C $(100 \text{ km})^{-1} \text{ h}^{-1}$. Although the observations indicate similar magnitudes and the same variations of wind and temperature fields in the frontal zone, insufficient resolution of the data leads to smaller estimates of frontogenesis terms.

The frontolytic region between the coastline and midshelf front cannot be simply explained by the distribution of surface-layer turbulent heat flux (Fig. 12) alone because the heat flux, in general, increases offshore to the western edge of the Gulf Stream. The dis-

tribution of turbulent sensible heat flux divergence (Fig. 14), however, shows that the region of maximum heating is close to the coastline and the leading edge of the turbulent heating is near the midshelf front. At this time, turbulent heating east of the midshelf front is not as prominent as before. Indeed, thermodynamic processes in the vicinity of the Gulf Stream are reaching steady state, characterizing the typical feature of a linear heating profile normally found in a convective PBL. Due to the offshore cold advection by the north-northeast wind behind the front, the western edge of the midshelf front appears to be the preferred location of coastal front formation.

Frontogenesis at upper levels is more complex because of the influence of the cloud microphysics. In general, frontolysis is dominated by the vertical tilting above 1 km with a maximum magnitude of 60°C $(100 \text{ km})^{-1} \text{ h}^{-1}$. With strong upward motions over the coastal front, differential adiabatic cooling would lead to large frontolysis. Contribution by the differential turbulent sensible heating to the frontogenesis is small [only 10°C $(100 \text{ km})^{-1} \text{ h}^{-1}$ as a maximum], and it is incapable of producing the modeled coastal frontogenetical band at 150 m. As mentioned before, coastal flow is still confluent along the low-level confluence axis at 1-km height, yielding a frontogenetical contribution up to 21°C $(100 \text{ km})^{-1} \text{ h}^{-1}$. This frontogenesis (by flow confluence) tends to maintain the low-level confluence axis, but counteracts only a small portion of the frontolysis by vertical tilting. The total frontogenetical function is thus very frontolytic above 1-km height, resulting in the shallowness of the coastal front as found by Ballentine (1980). The frontolysis by vertical tilting is more dominant at higher levels, especially in the concentrated updraft regions. However, the coastal rainbands do not dissipate because of the release of latent heat in the updrafts.

### d. Moist convection instability

Moist convection over the Gulf Stream region has a rapid development by 6 to 8 model integration hours, after which considerable clouds develop. The onset of intense clouds depends on the degree of the MBL modification and on whether moisture transport caused by turbulent fluxes has reached the lifting condensation level (LCL). Modification of the MBL is to provide a background atmosphere where clouds can develop easily once the updrafts reach the LCL. Consequently, the interactive effects of the cloud formation (with latent heat release) and the MBL turbulent transfer result in the rapid growth of the updrafts as discussed before. This meso$\beta$-scale flow instability appears to be linked to the conditional symmetric instability (CSI) for moist flow in a baroclinic zone (Hoskins 1974). Symmetric instability (SI) for dry flow can also be described as inertial instability on an isentropic surface of the at-
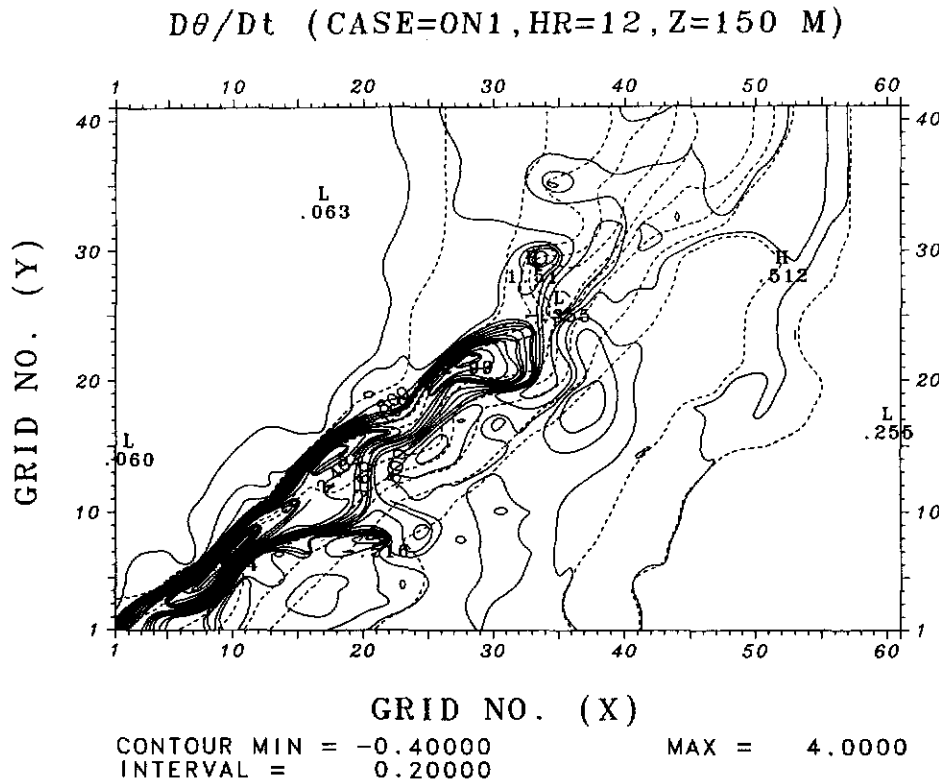
$D\theta/Dt$   ($CASE=ON1$, $HR=12$, $Z=150$ M)

FIG. 14. Differential turbulent sensible heating at 150 m AGL at 12 h. Solid lines represent heating regions with a contour interval 0.2°C h$^{-1}$. Surface temperature is also plotted for reference (represented by short dashed lines in a contour interval of 1°C).

CONTOUR MIN = −0.40000      MAX = 4.0000
INTERVAL = 0.20000

mosphere (Bennetts and Hoskins 1979; Emanuel 1979).

Linear theory shows that the presence of negative potential vorticity in dry flow would be indicative of SI (Hoskins 1974). Bennetts and Hoskins (1979) further indicated that CSI in moist flow could result from negative equivalent potential vorticity. The equivalent potential vorticity can be defined as

$$q_e = (f\mathbf{k} + \nabla \times \mathbf{V}) \cdot \nabla\theta_e \qquad (2)$$

where $f$ is the Coriolis parameter, $\mathbf{k}$ is a unit vector in the vertical direction, and $\mathbf{V}$ is the wind vector. It was shown that development of a moist slantwise convection in a frontal zone can be explained in terms of zero or negative $q_e$ (Emanuel 1985). This CSI indicator has also been used to explain the rainband formation in 2D cold frontal systems (Parsons and Hobbs 1983; Knight and Hobbs 1988). Regions of the cold front updrafts and rainbands were found to coincide well with the CSI zone where negative $q_e$ existed.

Applying the CSI theory to the coastal front (case ON1), one finds that the geometry of CSI is similar to that of convective instability (Fig. 11), that is, regions of negative or near-zero values of $\partial\theta_e/\partial z$ generally co-incide with negative $q_e$. Equation (2) can be expressed as

$$q_e = \frac{\partial\theta_e}{\partial x}\left(\frac{\partial w}{\partial y} - \frac{\partial v}{\partial z}\right) + \frac{\partial\theta_e}{\partial y}\left(\frac{\partial u}{\partial z} - \frac{\partial w}{\partial x}\right)$$
$$+ \frac{\partial\theta_e}{\partial z}\left(\frac{\partial v}{\partial x} + f - \frac{\partial u}{\partial y}\right) \qquad (3)$$

where the last term is the combined effects of convective instability and absolute vorticity (indicating inertial instability). Obviously, convective (or conditional) instability is only a special case of the CSI (see Bennetts and Hoskins 1979). A conditionally stable layer could induce CSI if the associated absolute vorticity is predominantly negative (thus regarded as inertial instability). In the simulated region, the oceanic baroclinicity is very large. According to Eq. (3), the CSI, however, could result in part, from the horizontal SST gradients in some regions with no apparent convective instability.

Scale analyses of Eq. (3) for the case ON1, however, indicate that in a highly convective zone the first two terms are much less than the last term. For example, from Figs. 7 and 8,

$$-\frac{\partial \theta_e}{\partial x}\left|\frac{\partial v}{\partial z}\right| \sim \frac{20°C}{100\ km}\frac{10\ m\ s^{-1}}{3\ km}$$

$$= 0.66 \times 10^{-6}\ °C\ m^{-1}\ s^{-1},$$

$$\frac{\partial \theta_e}{\partial y}\left|\frac{\partial u}{\partial z}\right| \sim -\frac{20°C}{100\ km}\frac{10\ m\ s^{-1}}{3\ km}$$

$$= -0.66 \times 10^{-6}\ °C\ m^{-1}\ s^{-1},$$

$$\frac{\partial \theta_e}{\partial z}\left|f+\frac{\partial v}{\partial x}-\frac{\partial u}{\partial y}\right| \sim -\frac{50°C}{5\ km}\frac{20\ m\ s^{-1}}{20\ km}$$

$$= -10 \times 10^{-6}\ °C\ m^{-1}\ s^{-1}.$$

Although the SST gradients in the baroclinic zone can be as large as $20°C/100$ km, the vertical gradient of $\theta_e$ near the surface can itself be large, making the third term dominant. Regimes of CSI are thus the same as those of convective instability. It appears that convective instability is a necessary precondition of CSI, as shown by our nonlinear numerical results and the linear theoretical results of Bennetts and Hoskins (1979).

According to the CSI theory (Bennetts and Hoskins 1979), dry perturbation motions will grow at a rate $\omega$ given by

$$\omega^2 = -f\left(f+\frac{\partial v}{\partial x}\right) + \frac{\left(\frac{g}{\theta_0}\frac{\partial \theta}{\partial x}\right)^2}{\left(\frac{g}{\theta_0}\frac{\partial \theta}{\partial z}\right)}, \qquad (4)$$

where $g$ is the acceleration of gravity and $\theta_0$ is the reference mean potential temperature. Knight and Hobbs (1988) replaced $\theta$ with $\theta_e$ in (3) to account for the growth rate of moist flow. Application of the linear CSI theory to the frontal system in their study, however, had its limitations because of the strong nonlinearity of the flow and explicit numerical diffusion. Their primitive equation model predicts only about one-sixth of the perturbation growth rate given by the linear theory. Since $w = w_0 \exp(\omega t)$ for flow instability, $\omega = \partial \ln w/\partial t$. The modeled updraft growth rate during the fastest development (Fig. 5) will thus lie between about $1 \times 10^{-4}\ s^{-1}$ to $4 \times 10^{-4}\ s^{-1}$ with $w_0 = 0.7$ m s$^{-1}$ at 7.7 h and $w = 2.7$ m s$^{-1}$ at 8.7 h. The $e$-folding time of the updraft growth is less than one hour, in agreement with the linear theoretical limit with similar CSI factors. Indeed, small explicit horizontal and vertical diffusion does not significantly influence the CSI growth rate which, however, can be reduced by insufficient horizontal resolution of numerical simulation (Bennetts and Hoskins 1979). Because of the vigorous convection in the baroclinic MBL, the CSI growth rate is not underestimated by our numerical results obtained using 12.5-km horizontal resolution. The predicted CSI growth rate for the 3D case (ON1) is similar to the 2D case result (Huang and Raman 1991b) and

is about one order larger than for the 2D cold frontal system (Knight and Hobbs 1988).

Application of (4) to the case ON1 can be valid only in the region of conditional stable layer (Bennetts and Hoskins 1979). Convective instability would dominate at low levels with strong turbulent mixing, destabilizing the MBL and producing weak updrafts over the baroclinic zone. In the cloudy region, CSI could be established more easily because of the near-neutral condition. The near-neutral condition is also close to the applicable limit of a hydrostatic model. In this region, $\partial \theta_e/\partial x$ has a typical value of about $4°C/100$ km (see Fig. 8 for the cross-sectional results). In order to satisfy the theoretical prediction, CSI will require $\partial \theta_e/\partial z$ on the order of about $0.33°C/km$ during the stage of the fastest development. As can be seen in Fig. 8, this small value of $\partial \theta_e/\partial z$ can result from the strong moist convection over the coastal front. However, it is not clear as to how the onset of CSI would depend on the degree of the generated baroclinicity in this region. The MBL-induced CSI over the coastal front differs from that in cold front systems that have well-defined baroclinicity of the basic state. Since CSI is based on the small perturbation assumption for linear flow, it cannot describe the precise instability in a nonlinear coastal circulation, particularly at later stages. Using a Lagrangian parcel method, Emanuel (1983) showed that CSI in nonlinear flow acts in a manner similar to that for linear flow. In fact, CSI at later times becomes considerably suppressed or even diminished in the nonlinear coastal flow (Fig. 5).

## 4. Northerly ambient flow: The Gulf Stream rainband

Large-scale northerly flow was observed off the Carolinas during 23–24 January 1986 just one day before the coastal frontogenesis. Figure 15 depicts the 23 January synoptic weather system. A low pressure center formed north of Maine in association with a cold front moving offshore. For this case (denoted as OF1, see Table 1), little rainfall over land was reported, while over ocean clouds were present (see GALE Field Program *Summary* edited by Drexel University). The distribution of the precipitation in the OF1 event differed significantly from that in the ON1 event due to different ambient wind directions. The circulation system for OF1 (an offshore cold air outbreak episode) moves away from the coastal region because of the offshore ambient forcing down the SST gradients. There is no steady-state circulation for the offshore flow with a wind speed of 7.5 m s$^{-1}$, in contrast to that for the calm wind conditions (Warner et al. 1990). To understand the dynamics of the offshore cold airflow on the formation of the oceanic cloud and/or rainbands, the same approach as in ON1 is used for OF1. All the model components and input for OF1 are the same as
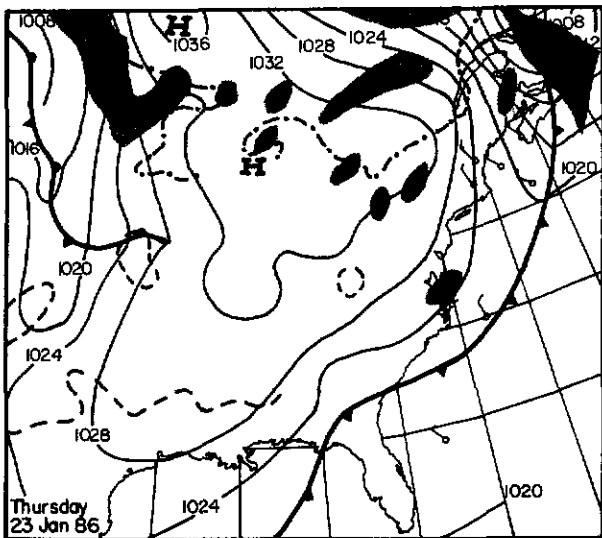
FIG. 15. The synoptic weather maps at 0700 EST
(1200 UTC) 23 January 1986.

for ON1, except that a geostrophic wind of $U_g = 0.1$ m s$^{-1}$ and $V_g = -7.5$ m s$^{-1}$ is used.

Figure 16 shows the time evolutions of the domain maximum and minimum vertical velocity and maximum surface-layer wind speed for the case OF1. Early rapid development of the circulations for the two cases are quite similar, except for a sudden growth of the updraft near 11 h for OF1. This later growth is possibly caused by the model upper and lateral boundary conditions as the clouds develop to the domain top and reach the eastern model boundary. Maximum surface-layer wind speed, despite the influence of the boundary conditions, is nearly in phase with the updrafts, indicating that the mesoscale circulation for offshore flow is primarily in response to low-level convergence.

The evolving surface-layer flow at 9 and 12 h is shown in Fig. 17. A strong convergence (indicated by the flow reversal) is well established at 9 h along the eastern 23°C SST contour marking the location of the circulation front. Behind the circulation front is accelerated flow with a maximum wind speed of 17 m s$^{-1}$ at 12 h, which then increases to 25.3 m s$^{-1}$ at 15 h. The front crosses the eastern 23°C isotherm and moves further offshore to the 21°C isotherms by 15 h. Stronger convergence can also be seen near the northeastern corner of the model domain, but it is probably due to the influence of the boundary conditions as mentioned before.

To investigate the vertical development of the flow, the wind fields at the CS1 cross section (normal to the coastline) are shown in Fig. 18. This cross section may not give the results at regions with the strongest updraft, but it would provide an insight into the structural features of the MBL in offshore flow conditions. In Fig.

18, a significant updraft appears at grid 37 (the leading edge of the front in Fig. 17) and is constrained within the lowest several levels (below 2 km) at 9 h. It becomes much stronger and higher to an altitude of about 4 km at 12 h. The updraft also does not tilt with height, similar to that in the coastal front discussed earlier (see Fig. 7). Associated with the developing updraft is the circulation front, which moves slowly downwind of the Gulf Stream. The development of the updraft is strongly related to the destabilization of the MBL as indicated by the cross-sectional results for $\theta_e$ and $q_e$ (Fig. 19). As can be seen in this figure, magnitudes of convection determine the developed height of the updraft.

The 3D configuration of the rainwater in the offshore flow circulation is of great interest. In response to flow convergence, a tall rainband up to 6–7-km height is produced at 9 h (Fig. 20), with a width less than 70 km. The rainband is along the eastern 23°C SST contour line (just east of the Gulf Stream core) and can be considered as "the Gulf Stream rainband" (Hobbs 1987). At 12 h, the Gulf Stream rainband is broadened to about 200 km in width, but its water loading remains
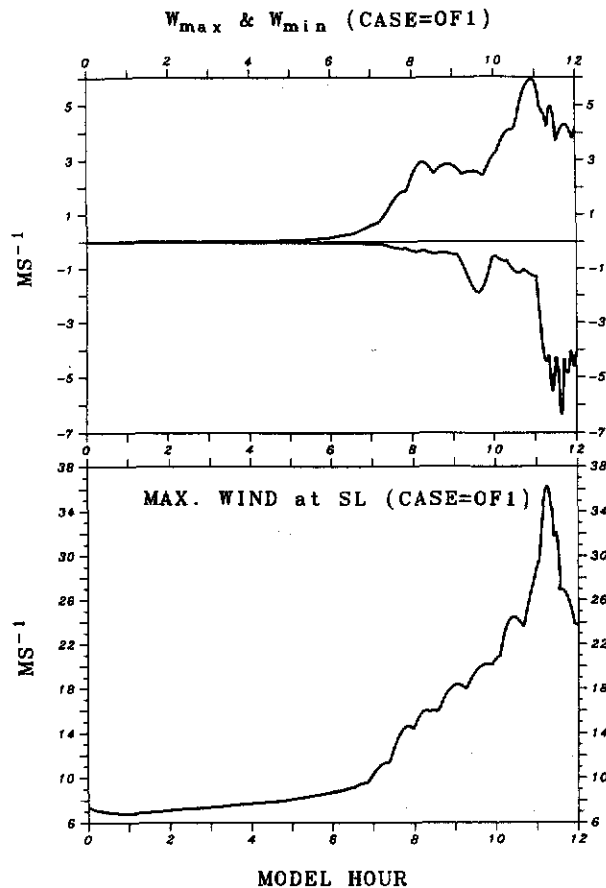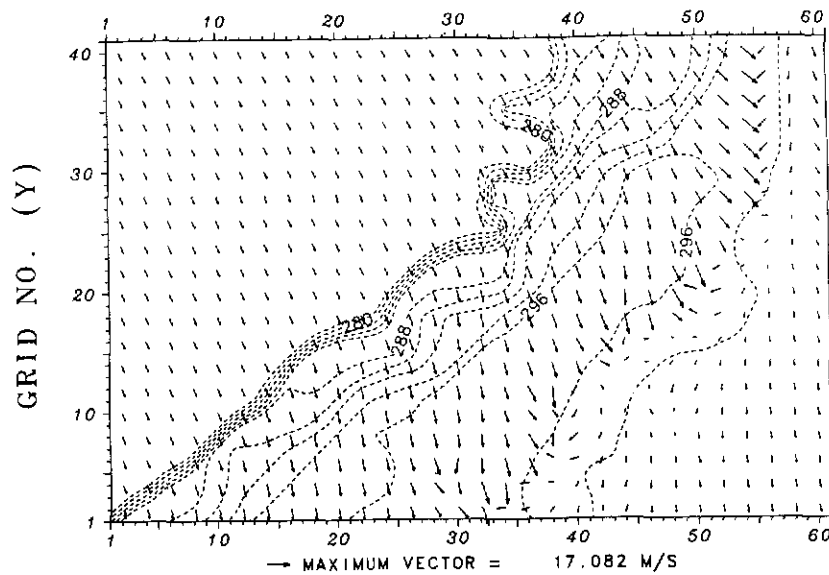


FIG. 16. As in Fig. 5 but for case OF1 (northerly offshore flow).

U & V (CASE=OF1,Z=150 M,HR=09)



→ MAXIMUM VECTOR =     17.082 M/S

U & V (CASE=OF1,Z=150 M,HR=12)



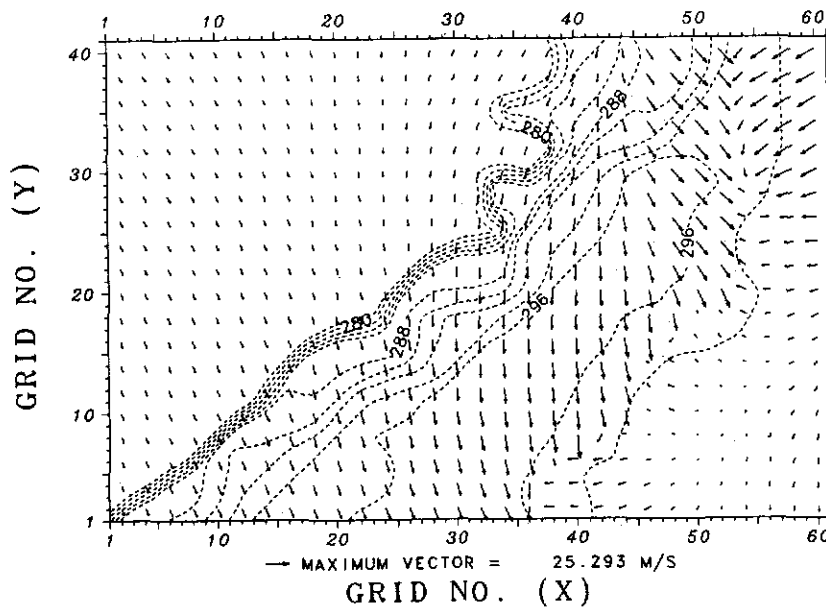→ MAXIMUM VECTOR =     25.293 M/S

GRID NO. (X)

FIG. 17. The results for $u$ and $v$ at 150 m AGL at 9 and 12 h for case OF1.
Others are the same as in Fig. 6.

largest along the eastern 23°C SST contour line. At 15 h, the Gulf Stream cloud/rainband develops to the model top (not shown) and spreads east of the Gulf Stream.

Distributions of the surface-layer turbulent sensible and latent heat fluxes in the offshore flow circulation are presented in Fig. 21. Variations of both sensible and latent heat fluxes closely follow the SST contour lines, except for the regions where locally accelerated wind exists. There is a region of larger gradient east of the eastern 23°C SST contour, supporting the geometry of the Gulf Stream rainband. In contrast to the maximum heating over the western side of the Gulf Stream core for the onshore flow, the eastern side is the location

WIND at CS1 (CASE=OF1,HR=09)
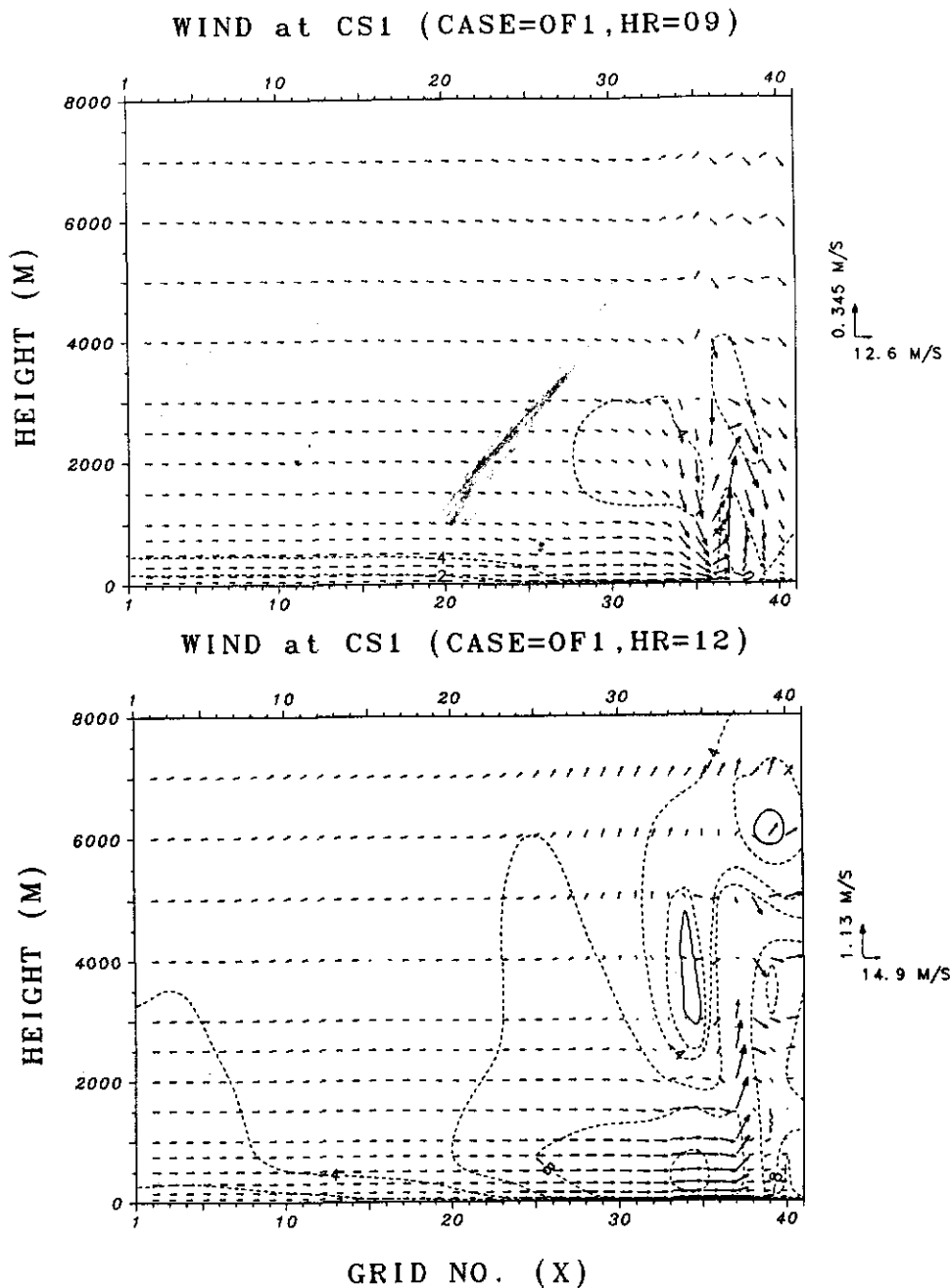


WIND at CS1 (CASE=OF1,HR=12)



GRID NO. (X)

FIG. 18. As in Fig. 7 but at 9 and 12 h for case OF1.

of maximum heating for the offshore flow. The value of maximum total heat flux (sensible plus latent heat fluxes) is around 1600–1700 W m$^{-2}$ for the offshore flow, about 300–400 W m$^{-2}$ larger than for the onshore flow. Observations during offshore cold air outbreaks (e.g., Akkarapuram and Raman 1988; Wayland and Raman 1989) also showed such large total heat fluxes over the Gulf Stream region.

## 5. Sensitivities of the circulation systems

### a. Ambient conditions

As shown previously, rainbands are produced west of the Gulf Stream core for the onshore flow and east of the Gulf Stream core for the offshore flow. The mesoscale circulation, hence, is predominantly determined by the direction of ambient flow. The model results
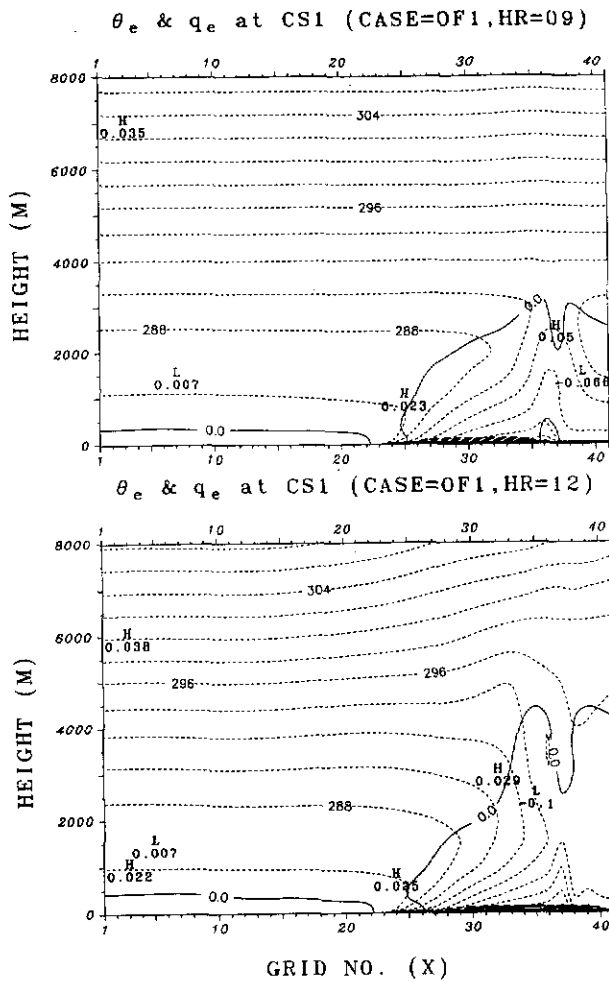
$\theta_e$ & $q_e$ at CS1 (CASE=OF1,HR=09)

$\theta_e$ & $q_e$ at CS1 (CASE=OF1,HR=12)

GRID NO. (X)

FIG. 19. As in Fig. 8 but at 9 and 12 h for case OF1.

the two flows increases quickly with time at the early stage of development but tends to decrease after the low-level convection reaches a quasi-equilibrium state. As shown before, regions of the minimum $q_e$ are found only at the lower levels (see Fig. 8). Through turbulent convection, differential ocean heating is capable of creating low-level atmospheric baroclinicity. Intense updrafts tend to appear only after sufficient baroclinicity has been generated in the MBL and the height of the MBL exceeds LCL as shown before. This can also be explained by Eq. (4), which indicates that perturbation motions (or updrafts) cannot grow without a horizontal temperature gradient of mean flow.

### b. Eddy Prandtl number

Eddy Prandtl number is defined as the ratio between eddy diffusivities for momentum and heat, that is, $Pr_t = K_M/K_\theta$. Normally, this number is less than unity under convective conditions. It has been found that the 2D circulation intensity during offshore cold air outbreak is sensitive to this ratio (Huang and Raman 1991b). The 2D results show that larger inverse eddy Prandtl numbers (that is, heat transfer is more vigorous than momentum transfer) would result in weaker updrafts. To further investigate this sensitivity, two additional cases, ON2 and OF2, were conducted (see Table 1). Cases ON2 and OF2 are identical to the cases ON1 and OF1, respectively, except that eddy Prandtl

tend to imply that the existence of onshore ambient flow is a precondition for coastal confluence and thus frontogenesis. Location of the coastal confluence is related to the magnitude of onshore surface-layer wind speed as revealed by our previous 2D sensitivity tests (Huang and Raman 1990). An increase in the onshore component of the surface-layer wind causes a further inland penetration of the confluence zone. On the other hand, Warner et al. (1990) found that calm wind conditions favor a convergence zone slightly west of the Gulf Stream core but smoothed SST gradients (commonly available) cause farther offshore location of the convergence zone and reduce the MBL front intensity significantly.
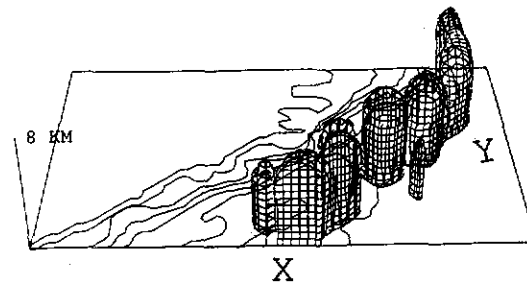
Although the direction of ambient flow predominantly determines the location of the circulation front, CSI is induced in both onshore and offshore flows. Table 2 summarizes the domain maximum and minimum equivalent potential vorticity $q_e$ at different times for both onshore and offshore flows. The instability of

RAIN WATER (CASE=OF1,HR=09)



RAIN WATER (CASE=OF1,HR=12)
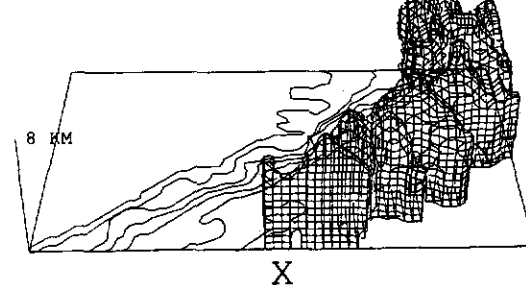


FIG. 20. As in Fig. 11 but at 9 and 12 h for case OF1.

S.H.  (CASE=OF1,Z=50 M,HR=12)



L.H.  (CASE=OF1,Z=50 M,HR=12)
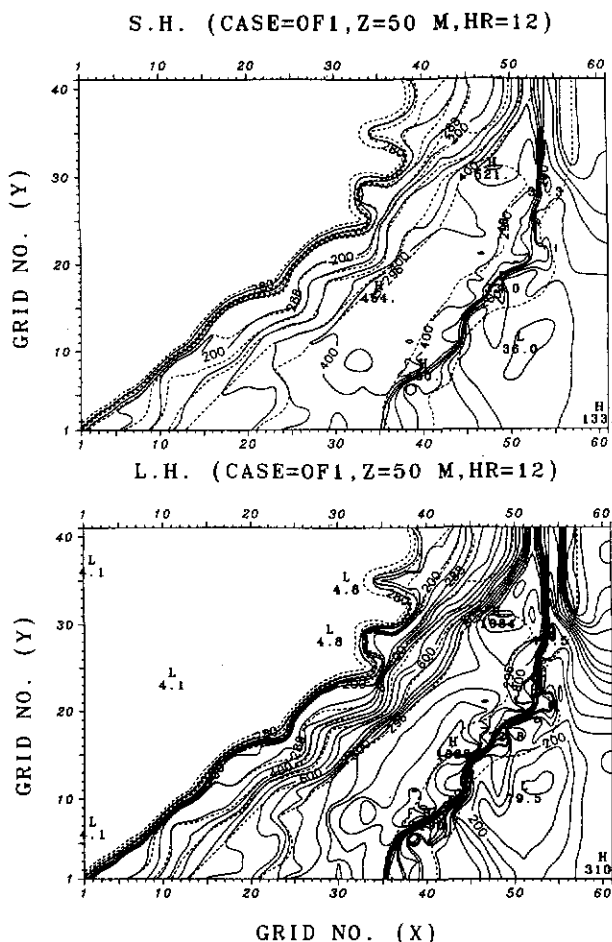


GRID NO. (X)

FIG. 21. As in Fig. 12 but for case OF1.

TABLE 2. Magnitudes of domain maximum and minimum equivalent potential vorticity ($q_e$) for cases ON1 (easterly onshore flow) and OF1 (northerly offshore flow). Here, $q_e = (f\mathbf{k} + \nabla \times \mathbf{V}) \cdot \nabla \theta_e$ where $\theta_e = \theta + L_c q/\pi$.

| | $q_e$ (°K m$^{-1}$ s$^{-1}$) | |
|---|---|---|
| Hour | Minimum | Maximum |
| Case ON1 (onshore flow) | | |
| 6 | $-1.02 \times 10^{-4}$ | $2.14 \times 10^{-5}$ |
| 9 | $-4.47 \times 10^{-4}$ | $5.27 \times 10^{-5}$ |
| 12 | $-5.46 \times 10^{-4}$ | $1.63 \times 10^{-4}$ |
| 15 | $-5.13 \times 10^{-4}$ | $1.53 \times 10^{-4}$ |
| Case OF1 (offshore flow) | | |
| 6 | $-1.11 \times 10^{-4}$ | $1.52 \times 10^{-5}$ |
| 9 | $-6.57 \times 10^{-4}$ | $1.10 \times 10^{-4}$ |
| 12 | $-6.74 \times 10^{-4}$ | $1.63 \times 10^{-4}$ |

Since the difference between the turbulence closures used in these cases is the determination of $Pr_t$, the vertical profiles of $K_M$ (bold) and $K_\theta$ (thin) at different places are plotted in Fig. 23 to examine their variations. Places were selected on the northwestern corner grid point (longer dashed), the southeastern corner grid point (dashed), and the grid point of maximum cloud-water loading. The values at the corner grids are used to provide upstream and downstream information relative to those in the developed circulation. For the onshore flow (ON2), magnitudes of $K_\theta$ and $K_M$ are found to be about two times larger than for ON1, but their distributions and the heights at which they vanish are quite similar. For the offshore flow, the variation between $K_M$ and $K_\theta$ caused by different determinations of Prandtl numbers is more prominent, especially at

number is not assumed to be a constant of unity, but determined by the level 2.5 formulation given by Mellor and Yamada (1982) (for details see Huang and Raman 1991b). To save computer time, the results at 6 h for ON1 and OF1 are used as the initial conditions for ON2 and OF2, respectively.

Figure 22 shows the evolution of the strongest updrafts and downdrafts for the four cases. During the integration period, vertical motions for the onshore and offshore flows, in general, are stronger with a constant Prandtl number of unity than with the larger inverse eddy Prandtl numbers given by the level 2.5 formulation. The 3D model results are similar to the ones given by the 2D model simulations (Huang and Raman 1991b). It should be noted, however, that the growth rates of the updraft for the four cases studied are not significantly sensitive to the variations in the eddy Prandtl numbers, which is consistent with the findings by Bennetts and Hoskins (1979). In addition, the location of the MBL convergence zone and the geometry of the developed rainbands are only slightly changed by differing eddy Prandtl numbers.

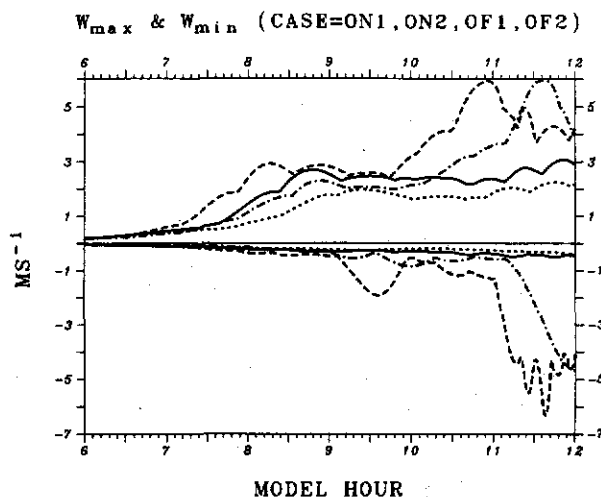$W_{max}$ & $W_{min}$  (CASE=ON1,ON2,OF1,OF2)



MODEL HOUR

FIG. 22. Time evolutions of oceanic domain maximum vertical velocity and minimum vertical velocity for case ON1 (solid lines), ON2 (shorter dashed), OF1 (longer dashed), and OF2 (dotted-dashed).
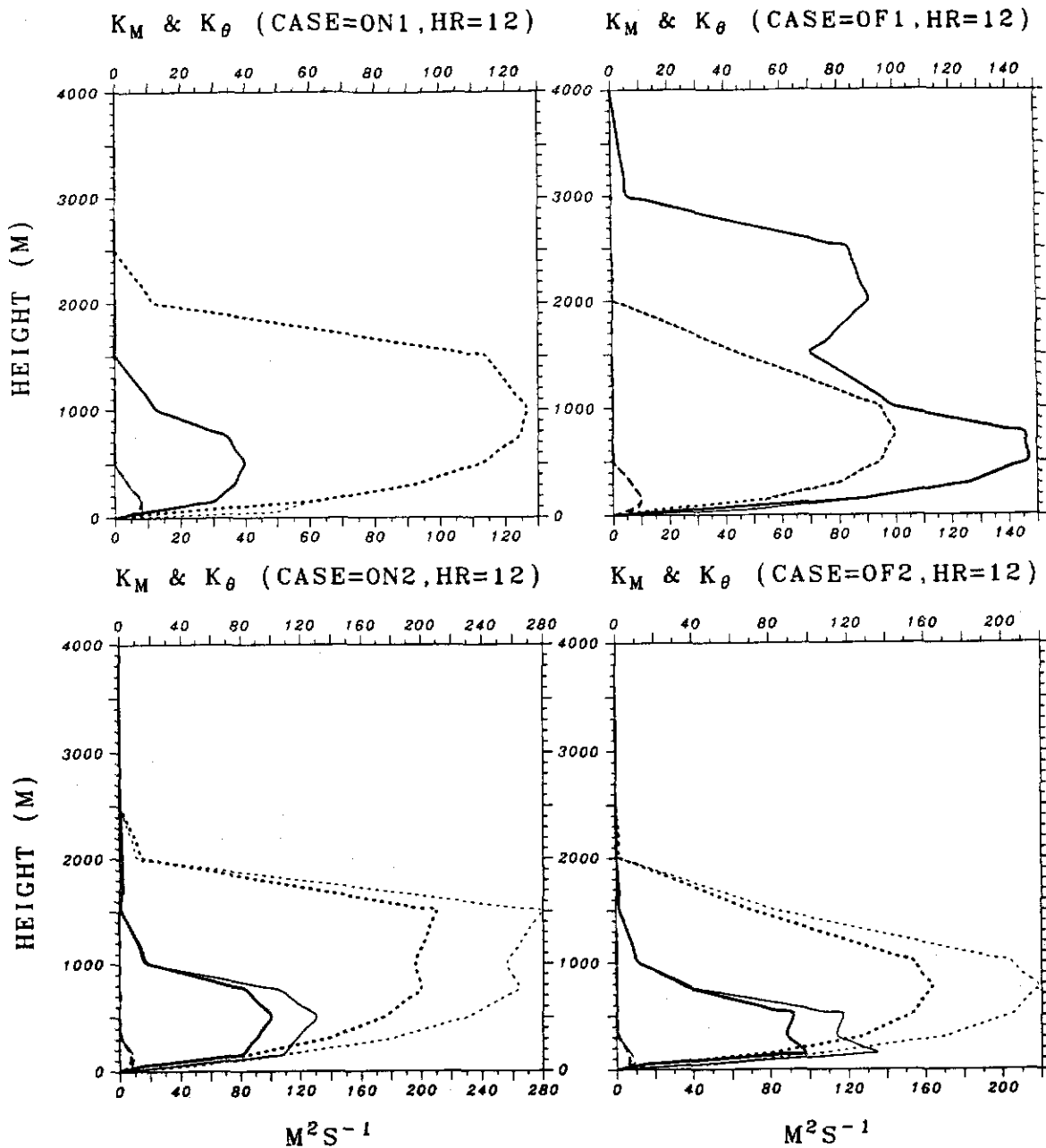
$K_M$ & $K_\theta$ (CASE=ON1, HR=12)        $K_M$ & $K_\theta$ (CASE=OF1, HR=12)

$K_M$ & $K_\theta$ (CASE=ON2, HR=12)        $K_M$ & $K_\theta$ (CASE=OF2, HR=12)

$M^2 S^{-1}$                          $M^2 S^{-1}$

FIG. 23. Vertical profiles of $K_M$ (bold lines) and $K_\theta$ (thin) at different locations at 12 h for cases (a) ON1, (b) OF1, (c) ON2, and (d) OF2. The locations are the northwestern corner grid (longer dashed lines) over ground and the southeastern corner grid (shorter dashed) over ocean in the model domain and the grid point of maximum cloud-water loading (solid lines).

the location of maximum cloud-water loading. Moreover, turbulence develops to a higher level for OF1 as compared to OF2. The results indicate that the role of eddy Prandtl number is important in the cloudy region where considerable shear can be generated.

Huang and Raman (1991b) found that upright convection tends to be associated with a larger inverse eddy Prandtl number for 2D flow. Slantwise convection could trigger larger vertical motions over the oceanic baroclinic zone as compared to upright convection.

Linear theoretical study (Emanuel 1979), however, indicates that inertial instability in hydrostatic flow with molecular diffusion tends to set in for larger Prandtl number beyond unity (the Prandtl number is defined here for molecular diffusivity); in contrast, it tends to set in for smaller Prandtl number below unity in nonhydrostatic neutral flow. In a systematic and theoretical investigation, Miller and Antar (1986) showed that with fixed Ekman, Rossby, and Richardson numbers baroclinic instability increases as the Prandtl number

(beyond unity) becomes larger. Since eddy diffusivity in the MBL is several orders stronger than molecular diffusivity and the MBL flow is highly nonlinear, model results may differ from theoretical results.

## 6. Conclusions

A mesoscale planetary boundary layer (PBL) numerical model is used to investigate mesoscale circulations over the Carolina coastal and Gulf Stream baroclinic zones. Two different types of the mesoscale circulations over this region are considered for simulation. The first is the coastal front initiated by the coastal contrasts in surface temperature and roughness; the second is an offshore cold air outbreak in response to the Gulf Stream baroclinicity. The two different phenomena are the results of different ambient flow directions.

Bosart (1975) indicated New England coastal fronts to be significantly related to the effect of differential frictional boundary layer in the presence of a synoptic high to the northeast. To understand the relative importance of boundary-layer transfer in the formation of the coastal front and the mesoscale circulation over the Gulf Stream region, a comprehensive turbulence closure scheme was used. The turbulence closure consists of two prognostic equations, one for the turbulent kinetic energy (TKE) and the other for turbulent dissipation ($\epsilon$). Eddy Prandtl number in this closure is determined by the level 2.5 formulation (Mellor and Yamada 1982). Huang and Raman (1991b) showed that this hybrid closure scheme can simulate the marine boundary layer (MBL) reasonably well.

Two types of idealized barotropic ambient onshore and offshore flows are investigated, which represent the synoptic conditions of the two phenomena (coastal front and cold air outbreak) observed during the 1986 Genesis of Atlantic Lows Experiment (GALE) IOP-2. For the easterly onshore ambient flow, a confluence zone appears over the midshelf front (west of the Gulf Stream) in response to the effects of the oceanic baroclinicity. This confluence zone is nearly parallel to the coastline and the SST isotherms. A shallow coastal front forms below 2 km as the cyclonic shear of ageostrophic flow becomes strong. The coastal frontogenesis is primarily maintained by the flow confluence. Differential turbulent heating produces a significant frontogenetical source along the coastline, counteracting the offshore cold air advection west of the front. Over the midshelf front off South Carolina where the confluence axis exists, differential turbulent heating actually contributes to frontolysis which, however, is compensated by the flow confluence. With prominent total frontogenesis, quasi-stationary rainbands are produced mainly along the coastal front, and develop much higher than the frontal depth. The tall rainbands are caused by cumulus convection over the cold air inland as the moisture tongue extends over the coastal front. The northern part of the front later encroaches inland as the cold air intensity over ground weakens due to onshore warm air advection.

The modeled coastal flow agrees well with the observations (Doyle and Warner 1990; Riordan 1990), suggesting that differential boundary-layer modification may be the main mechanism for the formation of the coastal front. That is, differences between the inland stable boundary layer and the convective MBL result in a thermal direct circulation that favors frontogenesis. Coastal thermal gradients are packed effectively by the onshore ambient flow. In general, local pressure gradients must be generated in the baroclinic zone in order to balance the effects of differential turbulent heating (Bosart 1975, 1981; Bosart and Lin 1984; Doyle and Warner 1990; Warner et al. 1990). For the northerly offshore ambient flow, the rainband therefore appears along the eastern edge of the Gulf Stream, which then moves slowly downstream in response to the locally generated atmospheric baroclinicity. This indicates the importance of the ambient wind direction in the determination of the mesoscale circulation front, as found in our previous 2D modeling studies (Huang and Raman 1990, 1991b).

Although the location of the mesoscale circulation front is determined mainly by the ambient wind direction, growth rates of the MBL updrafts for both onshore and offshore flows are quite similar. The fastest growth rate of the updrafts at earlier stages can be explained in terms of conditional symmetric instability (CSI). The e-folding time in the updraft growth is only about one hour, indicative of a very short time scale for the development of moist convection. The CSI mechanism in the MBL-induced mesoscale frontal rainband is similar to that in the rainband of a cold front (e.g., Knight and Hobbs 1988).

Coastal frontogenesis often provides a favorable situation for coastal cyclogenesis as in the case of the 1979 Presidents' Day Storm (Bosart 1981; Bosart and Lin 1984) and in the GALE IOP-2 case (Doyle and Warner 1990). The model results exhibit strong cyclonic shear associated with the coastal front; however, no closed cyclone was obtained in this study because of the limitation of the model domain and initial conditions. The wind shift in the coastal front tends to be embedded within a closed circulation, which then develops to an intense cyclone as in the IOP-2 event (Doyle and Warner 1990).

In addition to the boundary-layer differential heating, several conditions have been hypothesized in the literature that would induce or enhance coastal cyclogenesis: 1) ambient baroclinicity with/without a critical layer (Lin 1990), 2) a midtropospheric trough to the north (Uccellini et al. 1984, 1986), 3) curvature effects of the coastline (Bosart 1981), and 4) the CSI mechanism. The last mechanism, responsible for the fast growth of 2D mesoscale slantwise convection, may not be the exclusive one for triggering cyclogenesis in a 3D baroclinic MBL environment and deserves further attention.

Our future investigation will address the relationship between coastal frontogenesis and incipient cyclogenesis. A particular focus will be on the roles of the MBL and CSI in the cyclogenesis. Since the vertical and horizontal scales of the coastal cyclone are considerably larger than the embedded coastal front, a bigger model domain will be necessary. Development of the nested version of the model is in progress at the North Carolina Supercomputing Center, and the nested model will be used to investigate the IOP-2 cyclogenesis.

## REFERENCES

Akkarapuram, A. F., and S. Raman, 1988: A comparison of surface friction velocities estimated by dissipation and iterative bulk aerodynamic methods during GALE. *Geophys. Res. Lett.,* **15,** 401–404.

Ballentine, R. J., 1980: A numerical investigation of New England coastal frontogenesis. *Mon. Wea. Rev.,* **108,** 1479–1497.

Bennetts, D. A., and B. J. Hoskins, 1979: Conditional symmetric instability—a possible explanation for frontal rainbands. *Quart. J. Roy. Meteor. Soc.,* **105,** 945–962.

Bluestein, H. B., 1982: A wintertime mesoscale cold front in the Southern Plains. *Bull. Amer. Meteor. Soc.,* **63,** 178–185.

Bosart, L. F., 1975: New England coastal frontogenesis. *Quart. J. Roy. Meteor. Soc.,* **101,** 957–978.

——, 1981: The Presidents' Day Snowstorm of 18–19 February 1979: A subsynoptic-scale event. *Mon. Wea. Rev.,* **109,** 1542–1566.

——, and S. C. Lin, 1984: A diagnostic analysis of the Presidents' Day Storm of February 1979. *Mon. Wea. Rev.,* **112,** 2148–2177.

Dirks, R., J. P. Kuettner, and J. Moore, 1988: Genesis of Atlantic Lows Experiment (GALE): An Overview. *Bull. Amer. Meteor. Soc.,* **69,** 148–160.

Doyle, J. D., and T. T. Warner, 1990: Mesoscale coastal processes during GALE IOP 2. *Mon. Wea. Rev.,* **118,** 283–308.

Emanuel, K. A., 1979: Inertial instability and mesoscale convective systems. Part I: Linear theory of inertial instability in rotating viscous fluids. *J. Atmos. Sci.,* **39,** 1080–1097.

——, 1983: The Lagrangian parcel dynamics of moist symmetric instability. *J. Atmos. Sci.,* **40,** 2368–2376.

——, 1985: Frontal circulations in the presence of small moist symmetric stability. *J. Atmos. Sci.,* **42,** 1062–1071.

Hobbs, P. V., 1987: The Gulf Stream rainband. *Geophys. Res. Lett.,* **14,** 1142–1145.

Holt, T., S. Chang, and S. Raman, 1990: A numerical study of the coastal cyclogenesis in GALE IOP 2: Sensitivity to PBL parameterizations. *Mon. Wea. Rev.,* **118,** 234–257.

Hoskins, B. J., 1974: The role of potential vorticity in symmetric stability and instability. *Quart. J. Roy. Meteor. Soc.,* **100,** 480–482.

Huang, C. Y., 1990: *A Mesoscale Planetary Boundary Layer Numerical Model for Simulations of Topographically Induced Circulations.* Ph.D. dissertation, North Carolina State University, 253 pp.

——, and S. Raman, 1988: A numerical modeling study of the marine boundary layer over the Gulf Stream during cold air advection. *Bound.-Layer Meteor.,* **45,** 251–290.

——, and S. Raman, 1990: Numerical simulations of cold air advection over the Appalachian Mountains and the Gulf Stream. *Mon. Wea. Rev.,* **118,** 343–362.

——, and S. Raman, 1991a: Numerical simulation of January 28 cold air outbreak during GALE. Part I: The model and sensitivity tests of turbulence closures. *Bound.-Layer Meteor.,* **55,** 381–407.

——, and S. Raman, 1991b: Numerical simulation of January 28 cold air outbreak during GALE. Part II: The mesoscale circulation and marine boundary layer. *Bound.-Layer Meteor.,* **56,** 51–81.

——, and S. Raman, 1991c: A comparative study of numerical advection schemes, featuring a one-step modified WKL algorithm. *Mon. Wea. Rev.,* **119,** 2900–2918.

Kessler, E., 1969: On the distribution and continuity of water substance in atmospheric circulation. *Meteorological Monographs,* No. **32,** 1–84.

Klemp, J. B., and D. R. Durran, 1983: An upper boundary condition permitting internal gravity wave radiation in numerical mesoscale model. *Mon. Wea. Rev.,* **111,** 430–444.

Knight, D., and P. V. Hobbs, 1988: The mesoscale and microscale structure and organization of clouds and precipitation in midlatitude cyclones. Part XV: A numerical modeling study of frontogenesis and cold-frontal rainbands. *J. Atmos. Sci.,* **45,** 915–928.

Lin, Y. L., 1990: A theory of cyclogenesis forced by diabatic heating. Part II: A semigeostrophic approach. *J. Atmos. Sci.,* **47,** 1755–1777.

Marks, F. D., Jr., and P. M. Austin, 1979: Effects of the New England coastal front on the distribution of precipitation. *Mon. Wea. Rev.,* **107,** 53–67.

Mellor, G. L., and T. Yamada, 1982: Development of a turbulence closure model for geophysical fluid problems. *Rev. Geophys. Space Phys.,* **20,** 851–875.

Miller, T. L., and Antar, B. N., 1986: Viscous nongeostrophic baroclinic instability. *J. Atmos. Sci.,* **43,** 329–338.

Nielsen, J. W., 1989: The formation of New England coastal fronts. *Mon. Wea. Rev.,* **117,** 1380–1401.

Parsons, D. B., and P. V. Hobbs, 1983: The mesoscale and microscale structure and organization of clouds and precipitation in midlatitude cyclones. XI: Comparisons between observational and theoretical aspects of rainbands. *J. Atmos. Sci.,* **40,** 2377–2397.

Petterssen, S., 1936: A contribution to the theory of frontogenesis. *Geofys. Publ.,* **11,** 1–27.

Richwein, B. A., 1980: The damming effect of the Southern Appalachians. *Natl. Wea. Dig.,* **5,** 2–12.

Riordan, A. J., 1990: Examination of the mesoscale features of the GALE coastal front of 25–25 January 1986. *Mon. Wea. Rev.,* **118,** 258–282.

Sienkiewicz, J. M., J. D. Locatelli, P. V. Hobbs, and B. Geerts, 1989: The organization and structure of clouds and precipitation on the mid-Atlantic coast of the United States. Part II: The mesoscale and microphysical structure of a frontal system. *J. Atmos. Sci.,* **46,** 1349–1364.

Uccellini, L. W., P. J. Kocin, R. A. Petersen, C. H. Wash, and K. F. Brill, 1984: The Presidents' Day cyclone of 18–19 February 1979: Synoptic overview and analysis of subtropical jet streak influencing the pre-cyclogenetic period. *Mon. Wea. Rev.,* **112,** 31–55.

——, K. F. Brill, R. A. Petersen, D. Keyser, R. Aune, P. J. Kocin, and M. des Jardins, 1986: A report on the upper level wind conditions preceding and during the Shuttle *Challenger* (STS 51L) explosion. *Bull. Amer. Meteor. Soc.,* **67,** 1248–1265.

Wai, M. M., 1988: Modeling the effects of the spatially varying sea-surface temperature on the marine atmospheric boundary layer. *J. Appl. Meteor.,* **27,** 5–19.

——, and S. A. Stage, 1989: Dynamical analyses of marine atmospheric boundary layer structure near the Gulf Stream oceanic front. *Quart. J. Roy. Meteor. Soc.,* **115,** 29–44.

Warming, R. F., P. Kutler, and H. Lomax, 1973: Second- and third-order noncentered difference schemes for nonlinear hyperbolic equations. *AIAA J.,* **11,** 189–196.

Warner, T. T., M. N. Lakhtakia, and J. D. Doyle, 1990: Marine atmospheric boundary layer circulations forced by Gulf Stream sea surface temperature gradients. *Mon. Wea. Rev.,* **118,** 309–323.

Wayland, R., and S. Raman, 1989: Mean and turbulent structure of a baroclinic marine boundary layer during the 28 January 1986 cold-air outbreak (GALE86). *Bound.-Layer Meteor.,* **48,** 227–254.